Linear Frequency Domain Method for Load Control by Fluidic Actuation

Markus Widhalm[*]

German Aerospace Center (DLR), Braunschweig, 38108, Germany

Tobias Knopp[†]

German Aerospace Center (DLR), Göttingen, 37073, Germany

Vlad Ciobaca[‡]

German Aerospace Center (DLR), Braunschweig, 38108, Germany

Simulations of periodic fluidic excitations in the context of active flow control are performed using a frequency domain solver for the efficient prediction of global air loads. Frequency domain methods have become a viable choice whenever the disturbance of the flow is small and periodic, and can reduce the computational effort substantially in comparison to time-accurate unsteady simulations. Although time-accurate unsteady simulations resolve the entire spectrum of the flow, they suffer from a long transient phase and thus require an extensive use of computational resources. The goal is to extend the time-linearized frequency domain method of the DLR TAU-code toward load control by blowing fluidic actuators. This paper presents the set of discretized unsteady equations and associated boundary conditions for both the time accurate and frequency domain method. The applied time-linearized frequency method decouples each harmonic, forming a linear approach, which renders the sequential calculation of the individual harmonics to evaluate the time response of air loads. At first, blowing actuation for a two-dimensional airfoil with a single slot is considered for which constant as well as periodic excitations are used for validation and investigation purposes of air loads between the time-accurate and nonlinear frequency domain method. In addition, a 2-element high-lift wing with a flow separation on the trailing edge flap is simulated that demonstrates the good prediction quality of air load derivatives with the frequency domain method.

Nomenclature

Variables

f	frequency, Hz
$\mathbf{n}$	unit outward normal vector with components n_x, n_y and n_z
t	physical time, s
τ	dimensionless time
C_L	lift coefficient
α	incidence angle

Superscripts

‾	time-invariant mean state
ˆ	Fourier coefficient, perturbation amplitude
˜	time-dependent perturbation

---

[*]Research Engineer, Institute of Aerodynamics and Flow Technology, CASE branch, email:markus.widhalm@dlr.de.

[†]Research Engineer, Institute of Aerodynamics and Flow Technology, CASE branch

[‡]Research Engineer, Institute of Aerodynamics and Flow Technology, Transport Aircraft branch, Member AIAA.

American Institute of Aeronautics and Astronautics

Abbreviations

FRF Frequency response function
ARF Amplitude response function

I.   Introduction

Suction and blowing of air on aerodynamically heavily loaded surfaces to reduce structural loads in transonic flight conditions or to maximize lift at low speed flight has been highly attractive for many years. Decades of research have given insight into the air load behavior for active flow control (AFC) by steady or periodic excitations elaborately discussed by Greenblat and Wygnanski,[1] especially for periodic excitations. Global air loads of aircraft can be sufficiently modified without deploying movable control surfaces to adjust, for example the angle of attack in varying flight conditions. It is further an important feature, that the lifting surfaces are significantly less disrupted in terms of integration on the wing surface, except for installation difficulties. Therefore, numerous applications can be found for implementing AFC on aircraft or rotorcraft. Historically, this large area of research was dedicated to boundary layer control, so that the time-averaged mean flow is altered, Ref.[2] . Nowadays the focus has shifted to flow control with the global approach to use a reduced amount of energy (mass-flow) with a noticeable change of the reference flow without AFC. Flow control for airfoil aerodynamics may postpone or even prevent separation for example reducing aerodynamic stall for increasing maximum lift, Ref.[3–5] , or reducing the blade-vortex interaction on rotor blades, Ref.[6,7] Another viable application is the improved maneuverability such as roll control, Ref.[8]

It was demonstrated that oscillatory blowing can delay separation from a symmetrical airfoil more effectively than the steady blowing used traditionally for this purpose by Seifert and Pack.[9] Oscillatory suction and blowing are several times more efficient for lift than steady blowing and becomes particularly efficient if the excitation frequencies correspond to the most unstable frequencies of the free shear layer. Arrays of spanwise vortices are generated which are transported downstream and continuously mix with the shear layer. Hence, the frequency analysis of the flow around the lifting body has a significant influence for an effective active flow control. Considering that small changes in the onflow parameters can change radically the flow pattern around the body, it is critical to have a quick feedback to modify the parameters of the actuator.

The numerical treatment of fluidic actuators has its challenges. Actuators for complex configurations are mainly modeled in a simplified arrangement by considering a portion of the physical actuator, for example a portion of an actuation slot, neglecting the physical components of the actuators such as membranes, or switching valves. The size of an airfoil to a slot is by nature very different. Modeling of this arrangement for viscous flow simulations requires much experience in generating the computational grid so that the robustness of the numerical method is not overly affected by large changes in volume element sizes. In addition, the boundary layer resolution in the narrow slot has to cope with a wide range of flow conditions, ranging from zero up to two orders of magnitude in the jet velocity. Another numerical issue of periodic excitations is the simulation of unsteady turbulent flows by Reynolds-averaged approaches, and requires special attention for the treatment of motion and turbulent time-scales. To correctly capture all unsteady flow features, a proper time-resolution is required and the simulation has to last at least several periods to overcome the transient phase. Successful unsteady numerical simulations for high-lift multi-element airfoils with multiple slots on all three elements were investigated by Shmilovich and Yadlin,[10] and obtained a substantial gain in maximum lift by carefully locating the actuators. A similar numerical approach was followed by Ciobaca et al.[11] for a two-dimensional high-lift configuration, and this study was extended to a high-lift wing-body aircraft,[12] with both configurations pre-tested in a wind tunnel campaign. Schatz et al.[13] investigated separation control for high-lift devices by simulating different excitation modes and frequencies to identify optimal control parameters. The same group, with Hoell et al.[14] , extended this survey with detached-eddy simulations. It was shown in the works cited above that flow control physics is reproduced quite well by flow solvers. Subsequently, this leads to numerical optimization of active flow control parameters. Locations and blowing direction of multiple slots on the flap of a high-lift configuration are optimized by Nielsen and Jones[15] with a time-dependent adjoint technique.

For periodic excitations, frequency domain solvers have made major contributions in determining efficiently dynamic response data, which can be used to model the nonlinear time periodic flow by a small-disturbance approach. The effort for a time-accurate simulation of a flow problem can be reduced to about

a similar time scale of a steady-state simulation, and time-saving factors of up to two orders of magnitude are achieved. Frequency domain techniques can be utilized more efficiently to analyze a wide variety of performances, flight dynamic and aeroelastic stability problems to cover a broad frequency band. Applications to viscous flows range from blade-interaction in turbo machinery[16] or improving RANS-based aeroelastic instability predictions.[17, 18] The proposed Linear Frequency Domain (LFD) method[19] obtained good results for the prediction of dynamic responses for rigid body motions[20–22] at viscous transonic flow conditions.

In the current work, the LFD method for actuation is first investigated for a NACA 4412 airfoil with a single slot on the suction side with a perturbation on the blowing actuation velocity. Second, a high-lift wing with actuation on the trailing edge flap is studied with a similar blowing actuation setup. Both configurations are investigated for ambient viscous subsonic conditions and for various angles of attack. Derivatives of the lift coefficient are compared to their URANS counterparts for sinusoidal, half-wave rectified sine and pulse train jet velocity excitations for a multitude of frequencies. Fluidic periodic actuation is mostly based on pulsating signals, and as a result, contains higher harmonic components in the air load time response. The time-linearized small disturbance approach of the LFD decouples each harmonic, which is a simplification to the general description of the discrete Fourier transform of the nonlinear set of flow equations. In the following, a survey is conducted with the LFD, for the quality of reconstructing pulsed actuation in the time domain with the superposition of several harmonics. Time-reduction factors for pulsed actuation of up to two orders of magnitude are demonstrated in comparison with unsteady Reynolds-Averaged Navier-Stokes (URANS) simulations.

II.   Numerical Approach

The TAU flow solver[23, 24] uses the mass-weighted (Favre) averaged three-dimensional instantaneous Navier-Stokes equations, commonly referred to as the RANS equations, with numerous turbulence models to choose from. For this investigation, however, only the one-equation turbulence model of Spalart-Allmaras[25, 26] has been taken. The code is used to perform aerodynamic simulations for a wide range of Mach numbers and provides an extensive list of options and solution algorithms[27] for spatial discretizations on general mixed-element unstructured meshes. A finite volume approach is applied for solving the discretized RANS equations based on second-order accurate schemes. The edge-based method is generalized for three-dimensional unstructured meshes for which non-overlapping control volumes are bounded by an arbitrary number of constitutive faces. An Arbitrarian Lagrangian-Eulerian approach[28] is implemented to extend the applicability to mesh motions. Parallel scalability to many-core processors is achieved through domain decomposition and message passing communication.

The nondimensional time dependent compressible Navier-Stokes equations (URANS) can be written in a semi-discrete form as

$$\mathbf{M}\frac{\mathrm{d}\mathbf{W}(t)}{\mathrm{d}t} + \mathbf{R}(\mathbf{W}(t, \mathbf{u}_{\mathrm{jet}}(t))) = 0, \tag{1}$$

where $\mathbf{M} := \mathrm{diag}\,|\Omega_i|$ denotes the mass matrix with dimension of total number of grid nodes n_p. The state vector of conservative variables for each grid-node is given by $\mathbf{W}(t) := [\rho, \rho\mathbf{U}, \rho e, \rho\check{\nu}]^T \in \mathbb{R}^{N \times n_p}$ for $N = 6$ flow state variables with ρ being the density, $\mathbf{U} := [u(t), v(t), w(t)]^T$ is the velocity vector, e is the specific total energy and $\check{\nu}$ is the Spalart-Allmaras primitive working variable. $\mathbf{R} \in \mathbb{R}^{N \times n_p}$ denotes the spatial discretization of the convective and viscous flux density integrals. The blowing actuation velocity vector $\mathbf{u}_{\mathrm{jet}}(t)$ at the slot domain inflow is described as a combination of a mean velocity and a time-dependent periodic oscillation,

$$\mathbf{u}_{\mathrm{jet}}(t) = u_{\mathrm{jet}}(t)(-\mathbf{n}) = \bar{\mathbf{u}} + \tilde{\mathbf{u}}(t), \quad u_{\mathrm{jet}}(t) = \bar{u} + \tilde{u}(t), \tag{2}$$

where $u_{\mathrm{jet}}(t) > 0$ represents blowing, $u_{\mathrm{jet}}(t) < 0$ represents suction, and $\bar{u}$ is the magnitude of the mean velocity. $\mathbf{n}$ is the outward facing unit normal vector per face at the slot domain inflow. The oscillatory part of the jet velocity component is a function describing various periodic shapes of the velocity signal, and by setting $\tilde{u}(t) = 0$ the actuation reduces to a constant blowing or suction.

II.A.   Temporal Discretization

The temporal discretization is based on Jameson's[29] dual-time stepping scheme for the time-accurate solution of the RANS equations. Using an implicit multi-stage backward differential formula (BDF) discretization

American Institute of Aeronautics and Astronautics

in time, a large set of nonlinear equations is formed and marched in pseudo time to steady state for each physical time step using a geometric multigrid algorithm.[30, 31] Applications to arbitrary mesh motions have to preserve a time-accurate conservative scheme, which is satisfied using an approximation of the Geometric Conservation Law (Thomas and Lombard[32]).

II.B.   Actuation Boundary Condition

The physical constraints of the problem are combined with information from the interior of the domain to evaluate the fluxes on the boundary. That means, depending on the flow into the domain (blowing) and flow out of the domain (suction) a certain amount of state variables are extrapolated according to the theory of characteristics. In the present implementation, the boundary condition is divided into purely suction or blowing, as well as an option for applying zero net mass synthetic jets, Ref.[33, 34]
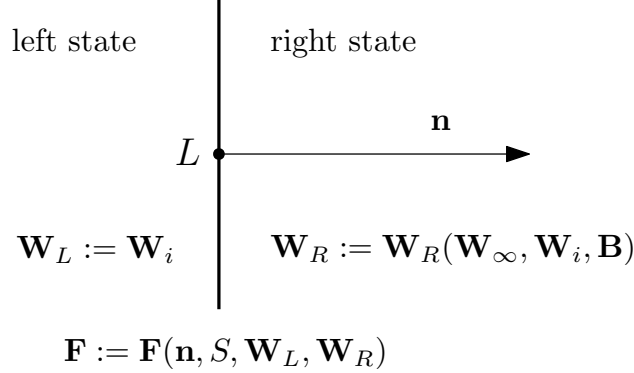

$$\mathbf{F} := \mathbf{F}(\mathbf{n}, S, \mathbf{W}_L, \mathbf{W}_R)$$

Figure 1. Flux and boundary states, L is the left (boundary/interior) state and R is the right (virtual/exterior) state.

As shown in fig. 1, the flux at the boundary ($\mathbf{F} := \mathbf{F}(\mathbf{n}, S, \mathbf{W}_L, \mathbf{W}_R)$) is composed of the left and right states ($\mathbf{W}_L$ and $\mathbf{W}_R$), the direction or normal vector, $\mathbf{n}$, and the face area, S. The left state is equal to the interior state, $\mathbf{W}_i$, and the right state is a function of the interior state, $\mathbf{W}_i$, the free-stream, $\mathbf{W}_\infty$, and/or user-specified parameters, $\mathbf{B}$, depending on the boundary condition. The TAU-code is a node-centered scheme, the left-side L is the boundary node at the physical domain, and the right-side R is a virtual or ghost node. To gain an appropriate boundary flux for the transport of quantities through the boundary, the flux is based on a first order scheme; thus, a first order Roe[35] scheme is used which is equivalent to a central differencing scheme with a first order matrix dissipation.[36] The convective flux evaluation on the boundary for face ij with adjacent grid nodes i and j can be written as

$$\mathbf{F}_{ij,\mathrm{Roe}}\mathbf{n}_{ij} = \mathbf{F}_{ij}^c\mathbf{n}_{ij} - \mathbf{D}_{ij}, \quad \mathbf{F}_{ij}^c = \frac{1}{2}(\mathbf{F}_i^c(\mathbf{W}_i) + \mathbf{F}_j^c(\mathbf{W}_j)),$$

$$\mathbf{F}_k^c\mathbf{n}_{ij} = \begin{pmatrix} \dot{m}_k \\ \dot{m}_k\mathbf{U}_k + p_i\mathbf{n}_{ij} \\ \dot{m}_k h_k \\ \dot{m}_k\breve{\nu}_k \end{pmatrix}, \quad \dot{m}_k = \rho_k\mathbf{U}_k\mathbf{n}_{ij}, \quad k = i, j,$$

$$\mathbf{D}_{ij} = |\mathbf{A}_{ij}^{\mathrm{Roe}}|\left[\frac{1}{2}\left(\mathbf{W}_j - \mathbf{W}_i\right)\right], \quad \mathbf{A}_{ij}^{\mathrm{Roe}} := \frac{\partial(\mathbf{F}_{ij}^c\mathbf{n}_{ij})}{\partial\mathbf{W}}[\mathbf{W}^{\mathrm{Roe}}],$$

(3)

where $\dot{m}$ is the mass flux through the surface area S_{ij}. The static pressure p and temperature T is related to the equation of state by $p/\rho = T$, and the specific total enthalpy can be evaluated with $H = E + p/\rho$. $\mathbf{W}_i := \mathbf{W}_R = (\rho_\infty, \rho_\infty\mathbf{u}_{\mathrm{jet}}(t), \rho_\infty e, \rho_\infty\breve{\nu})^T$ is the known state vector of conservative variables evaluated with given actuation boundary values.

The construction of matrix $\mathbf{A}_{ij}^{\mathrm{Roe}}$ is described in detail by Langer,[37] and $\mathbf{W}^{\mathrm{Roe}}$ denotes a Roe averaging[35] of the flow variables. Applying an Eigendecomposition for $\mathbf{A}_{ij}^{\mathrm{Roe}}$ results in three matrices which can be used to define

$$|\mathbf{A}_{ij}^{\mathrm{Roe}}| := \sum_m^{N_m} |\lambda_m|\mathbf{g}_m\mathbf{q}_m.$$

(4)

American Institute of Aeronautics and Astronautics

The two matrices $\mathbf{g}$ and $\mathbf{q}$ are composed of eigenvectors of the flux Jacobian. λ_m is a diagonal matrix containing the characteristic eigenvalues of the flow:

$$\lambda_m = \mathrm{diag}\,(\lambda_{ij}^+, \lambda_{ij}^-, \lambda_{ij}^n, \ldots, \lambda_{ij}^n). \tag{5}$$

The components of the eigenvalue matrix are

$$\begin{aligned}
\lambda_{ij}^+ &= \mathbf{U}_{ij}\mathbf{n}_{ij} + S_{ij}a_{ij}, \\
\lambda_{ij}^- &= \mathbf{U}_{ij}\mathbf{n}_{ij} - S_{ij}a_{ij}, \\
\lambda_{ij}^n &= \mathbf{U}_{ij}\mathbf{n}_{ij}.
\end{aligned} \tag{6}$$

where $a_{ij} := 0.5(a_i + a_j)$ is the speed of sound.

The simplest handling of the turbulent quantity $\check{\nu}$ in Eq. (3) is by extrapolation from the interior domain to obtain the eddy-viscosity closure. However, an empirical relation for the eddy-viscosity from experimental data for rounded jets is available from Hussein et al.[38] . The turbulent viscosity at the actuation boundary can be evaluated by

$$\check{\nu}_t^{(b)} =: \check{\nu}_t^{(b)}(\mathbf{u}_{\mathrm{jet}}) = 0.11\sqrt{\frac{2}{3}}\,\mathrm{Tu}\,\frac{1}{2}D_{\mathrm{jet}}\,|\mathbf{u}_{\mathrm{jet}}|, \tag{7}$$

and the jet turbulence intensity $\mathrm{Tu}^2 = 0.0053$ has been taken from Hussein's experiment, and D_{jet} is the slot width. The complete derivation of Eq. (7), starting from the turbulent fluctuation to the finally derived $\check{\nu}_t^{(b)}$, can be found in Knopp[34] .

The linearization of the flux function in Eq. (3) is written as the change in the flux function, F, with respect to the state vector, $\mathbf{W}$, on the boundary node denoted as left side:

$$\left.\frac{\partial\mathbf{F}}{\partial\mathbf{W}}\right|_L = \frac{\partial\mathbf{F}}{\partial\mathbf{W}_L} + \frac{\partial\mathbf{F}}{\partial\mathbf{W}_R}\frac{\partial\mathbf{W}_R}{\partial\mathbf{W}_L}. \tag{8}$$

The first two derivatives, $\partial\mathbf{F}/\partial\mathbf{W}_L$ and $\partial\mathbf{F}/\partial\mathbf{W}_R$, are the flux Jacobians for the numerical flux function on the virtual node (R) and at the boundary node (L). The flux Jacobian terms of Roe's scheme were derived analytically and handcoded term-by-term. Since the pressure is extrapolated for the blowing boundary condition, the matrix of derivatives $\partial\mathbf{W}_R/\partial\mathbf{W}_L$ has only entries in the fifth row $\partial\mathbf{W}_{R,5}/\partial\mathbf{W}_L = [q^2/2, \rho\mathbf{U}, 1/(\gamma-1), 0]$ and $q = (u^2 + v^2 + w^2)$.

Variables with dimensions are denoted by the superscript $\star$. Non-dimensional variables are denoted without any super- or subscript. Freestream values are denoted by the subscript ∞. The equations relating the dimensional to the non-dimensional flow-field variables are as follows:

$$\begin{aligned}
\rho^\star &= \rho\rho_\infty^\star, \quad \mathbf{U}^\star = \mathbf{U}a_\infty^\star, \quad p^\star = pp_\infty^\star, \quad T^\star = TT_\infty^\star = \frac{a_\infty^2}{\gamma}T_\infty^\star, \\
\rho_\infty &= 1, \quad p_\infty = 1, \quad T_\infty = 1, \quad a_\infty^2 = \gamma, \quad U_\infty = M_\infty a_\infty = M_\infty\sqrt{\gamma}, \\
[u_\infty, v_\infty, w_\infty]^T &= \mathbf{T}_{ba}[U_\infty, 0, 0]^T, \quad \mathbf{T}_{ba} = \begin{pmatrix} \cos\alpha\cos\beta & -\cos\alpha\sin\beta & -\sin\alpha \\ \sin\beta & \cos\beta & 0 \\ \sin\alpha\cos\beta & -\sin\alpha\sin\beta & -\cos\alpha \end{pmatrix} \\
e &= c_V T, \quad h = c_P T, \quad c_P = \frac{\gamma}{\gamma-1}, \quad c_V = \frac{1}{\gamma-1}, \quad R = 1\,.
\end{aligned} \tag{9}$$

The specific heat capacities are denoted as c_P and c_V, and R is the specific gas constant, and a_∞ is the speed of sound.

II.C. Frequency Domain Method

Postulating the considered actuation velocity time-dependent deflection to be of small amplitude, the flow response to the excitation can be considered to be predominately dynamically linear. Thus, higher order time-dependencies in the flow response can be neglected, allowing it to be separated into a time-invariant

American Institute of Aeronautics and Astronautics

mean state and a time-dependent small perturbation. On this basis, $\mathbf{W}$ can be linearized about an individual grid node's steady-state location using a Taylor-series expansion, that terminates after the first-order term:

$$\mathbf{W}(t) \approx \overline{\mathbf{W}} + \widetilde{\mathbf{W}}(t), \quad \|\widetilde{\mathbf{W}}\| \ll \|\overline{\mathbf{W}}\|, \tag{10}$$

$$\mathbf{u}_{\text{jet}}(t) \approx \bar{\mathbf{u}} + \tilde{\mathbf{u}}(t), \quad \|\tilde{\mathbf{u}}\| \ll \|\bar{\mathbf{u}}\|, \tag{11}$$

$$\mathbf{R}(\mathbf{W}(\mathbf{u}_{\text{jet}}(t))) \approx \overline{\mathbf{R}}(\overline{\mathbf{W}}(\bar{\mathbf{u}})) + \widetilde{\mathbf{R}}(\overline{\mathbf{W}}(\bar{\mathbf{u}}), \widetilde{\mathbf{W}}(\tilde{\mathbf{u}})). \tag{12}$$

Note, that $\overline{\mathbf{R}} = 0$ is neglected, which represents the steady-state solution, and the remaining term $\widetilde{\mathbf{R}}$ is transferred into the frequency domain. The perturbations are expressed in terms of a Fourier series and considering merely a first harmonic excitation and response

$$\begin{aligned} \mathbf{W} - \overline{\mathbf{W}} &\approx \widehat{\mathbf{W}}\, e^{i\omega t}, \quad \widehat{\mathbf{W}} \in \mathbb{C} \\ \mathbf{u} - \bar{\mathbf{u}} &\approx \hat{\mathbf{u}}\, e^{i\omega t}, \quad \hat{\mathbf{u}}_{\text{jet}} \in \mathbb{C} \end{aligned} \tag{13}$$

where $\omega = 2\pi f$ denotes the base angular velocity, which is in nondimensionalized form the reduced frequency $k = \omega l_{\text{ref}}/U_\infty$ introducing the reference chord length l_{ref} and the freestream velocity U_∞. Applying Eqs. (10)-(12) to Eq. (1) by neglecting higher order terms yields a separate linear system of equations linearized at steady-state conditions $(\overline{\mathbf{W}}, \bar{\mathbf{u}})$ for one harmonic excitation in the frequency domain. Thus, Eq. (1) becomes

$$\left[ik\mathbf{M} + \frac{\partial \mathbf{R}}{\partial \mathbf{W}} \right] \widehat{\mathbf{W}} = -\frac{\partial \mathbf{R}}{\partial \mathbf{W}} \frac{\partial \mathbf{W}}{\partial \mathbf{u}_{\text{jet}}} \hat{\mathbf{u}}_{\text{jet}}. \tag{14}$$

$\hat{\mathbf{u}}_{\text{jet}}$ is the known complex-valued description of the actuator jet velocity and thus, the system of equations can be solved for $\widehat{\mathbf{W}}$. Note, that the right-hand side of Eq. (14) is defined on the actuator inlet boundary only. With that approach, only the flux Jacobian derivatives per grid-node, $\partial \mathbf{R}/\partial \mathbf{W} \in \mathbb{R}^{N \times N}$, are necessary, and are derived analytically, Ref.[22, 39] The derivative $\partial \mathbf{W}/\partial \mathbf{u}_{\text{jet}} \in \mathbb{R}^{N \times 3}$ is the linearization of the right-side state variables in Eq. (8) with respect to the actuation jet velocity. It is defined only at the actuation boundary for the virtual node, and with the velocity in Eq. (2), it is written as

$$\left. \frac{\partial \mathbf{W}}{\partial \mathbf{u}_{\text{jet}}} \right|_R = \begin{bmatrix} \mathbf{0} \\ \rho \mathbf{I} \\ \mathbf{0} \\ \rho \, d\check{\nu}_t^{(b)} \end{bmatrix}, \quad d\check{\nu}_t^{(b)} = \frac{\partial \check{\nu}_t^{(b)}}{\partial \mathbf{u}_{\text{jet}}} = 0.11 \sqrt{\frac{2}{3}}\, \text{Tu}\, \frac{1}{2} D_{\text{jet}} \begin{cases} \mathbf{n}^T, & u_{\text{jet}} > 0 \\ -\mathbf{n}^T, & u_{\text{jet}} < 0 \end{cases} \tag{15}$$

where $\mathbf{I} \in \mathbb{R}^{3 \times 3}$ is a unitary matrix. Since perturbations of the actuation velocity are modeled with harmonics, the general description is written as

$$\begin{aligned} \tilde{\mathbf{u}}(\tau) &= \hat{\mathbf{u}} \sin(k\tau) = \hat{\mathbf{u}}\, \text{Im}(e^{ik\tau}), \quad \tau = \frac{U_\infty}{l_{\text{ref}}} t, \\ \hat{\mathbf{u}}_{\text{jet}} &= -i\hat{u}(-\mathbf{n}), \end{aligned} \tag{16}$$

where $\hat{u}$ denotes the magnitude of the excitation of the actuation velocity, and τ is the non-dimensional time.

All air load coefficients depend on the surface pressure c_p and skin friction coefficient $\mathbf{c}_f$, and the determination of $\hat{c}_p$ and $\hat{c}_f$ is provided in a further step to obtain the Fourier coefficients of the air loads, $\widehat{C}_i, i = L, D, m$. After receiving the solution state vector in conservative formulation it will be transformed into a primitive state vector to calculate real and imaginary pressure and skin friction coefficient distributions on the surface grid nodes. Quantities of interest are computed from $\widehat{\mathbf{W}}$ such as

$$C_i(t) := C_i(t, c_p(t), c_f(t)) \Rightarrow \widehat{C}_i := \widehat{C}_i(\hat{c}_p, \hat{\mathbf{c}}_f),$$

$$c_p = \frac{p_{\text{wall}} - p_\infty}{\frac{1}{2}\rho_\infty U_\infty^2}, \quad \hat{c}_p := \hat{c}_p(\hat{p}) = \frac{2\hat{p}}{\rho_\infty U_\infty^2}, \quad \hat{p} = \frac{\partial p}{\partial \mathbf{W}} \widehat{\mathbf{W}},$$

$$\mathbf{c}_f = \frac{\boldsymbol{\tau}\mathbf{n}}{\frac{1}{2}\rho_\infty U_\infty^2}, \quad \hat{\mathbf{c}}_f := \hat{\mathbf{c}}_f(\hat{\boldsymbol{\tau}}) = \frac{2\hat{\boldsymbol{\tau}}\mathbf{n}}{\rho_\infty U_\infty^2}, \quad \hat{\mathbf{c}}_f = \frac{\partial \boldsymbol{\tau}}{\partial \mathbf{W}} \widehat{\mathbf{W}}, \tag{17}$$

and p_{wall} denotes the pressure at the wall. Freestream values ρ_∞, U_∞ and p_∞ are density, velocity and pressure, respectively. $\boldsymbol{\tau}$ denotes the shear-stress tensor.

American Institute of Aeronautics and Astronautics

If the velocity excitation in time is not purely harmonic, like for a periodic pulse signal for example, or if the global air load coefficient's time response is not covered by the fundamental frequency f_0 (the nth Fourier coefficient does not fall off exponentially), then the approach of superposition with N harmonics is a viable approach. First, the actuation velocity signal is transformed into the frequency domain with a Fast Fourier Transform[40] to determine the maximum number of harmonics N_h so that the time signal can be restored to some degree. Applying the LFD sequentially for each harmonic, the time response of the global air load coefficients $C_i(\tau)$ can be recovered by

$$C_i(\tau) = \bar{C}_i + \sum_{n=0}^{N_h-1} \text{Re}\left(\Phi(nk_0)\widehat{C}_{i,n}\, e^{i2\pi nk_0\tau}\right), \quad n \in \mathbb{N}, \tag{18}$$

where $\bar{C}_i$ is the mean value derived from the steady-state simulation and $\widehat{C}_{i,n}$ are the complex-valued Fourier coefficients evaluated for N_h frequencies with the LFD. The $\Phi(nk_0)$ are the complex-valued weighting functions obtained from the Fast Fourier Transform of the actuation jet velocity signal, and are multiplied with the Fourier coefficients.

The most challenging part is to solve the large complex valued linear system, Eq. (14). Particularly, for viscous separated flows and small reduced frequencies, experience has shown that the linear system often becomes ill-conditioned and the iterative procedure may stall or diverge. Employing advanced techniques is therefore a necessity, such as Krylov-GMRES[41] with an Incomplete Lower-Upper (ILU)[42] preconditioning. Apparently, an ILU preconditioner based on a modified first and second order accurate flux Jacobian following the approach in Ref.[43,44] and extensions of the baseline GMRES,[45] increases the robustness of the method substantially.

III.   Actuation Signals

Conventional shapes or signals for the jet velocity during one actuation cycle can be represented by continuous or pulsating variations. The selection of signals includes three forms, the first of which represents a harmonic oscillation. Two additional actuation signals are considered, a half-wave rectified sine and a pulse train actuation jet velocity.

(a) Type of signals, $\bar{u}$, $\hat{u}$

(b) Magnitudes of the DFT(u(t)) for the half-wave rectified sine (red) and pulse train (blue) jet velocity signal.
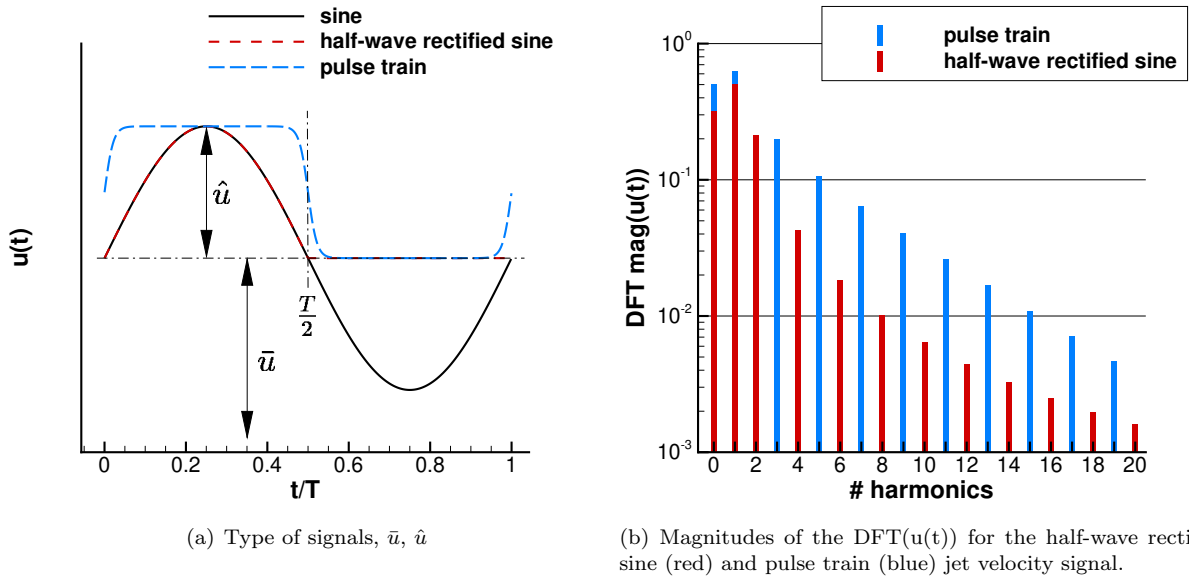
Figure 2. Excitation signals for the actuation jet velocity and the discrete Fourier transform (DFT) of the half-wave rectified sine and pulse train.

Figure 2 describes the dynamic excitation shapes of the actuation jet velocity, u_{jet}, composed of a mean jet velocity part, $\bar{u}$, and an oscillating jet velocity part, $\tilde{u}$, (Eq. (2)). The description of the actuation jet

velocities in fig. 2(a) is

$$\text{sine}: \quad u_{\text{jet}} = \hat{u}\sin\omega t, \quad 0 < t \leq T,$$

$$\text{half-wave rectified sine}: \quad u_{\text{jet}} = \begin{cases} \hat{u}\sin(\omega t), & 0 < t \leq t_c, \\ 0, & t_c < t \leq T, \end{cases}$$

$$\text{pulse train}: \quad u_{\text{jet}} = \begin{cases} \hat{u}, & 0 < t \leq t_c, \\ 0, & t_c < t \leq T, \end{cases} \tag{19}$$

where t_c is the time of the actuation duty cycle and is taken for all investigations to be half of the period, $t_c = T/2$. The pulse train actuation velocity can be applied with smoothing at the discontinuities introduced by Knopp.[34] Signals in the time domain can be represented by a series of sines. A common applied algorithm is the Fast Fourier Transform. It takes a signal and breaks it down into sine waves of different amplitudes and frequencies. The discrete Fourier transform is then a set of fundamental and harmonic components. The first jet velocity in Eq. (19) describes a harmonic signal and the second two are related to a discontinuous velocity distribution. An harmonic signal in the frequency domain is represented entirely by its fundamental frequency, so there is no zero frequency component. Since the latter two are discontinuous signals, the Gibb's phenomenon, apparent around $t/T = 0, T/2$, allows the restoration of the time signal only to a certain degree. For this reason, the reconstruction of the time signals for the half-wave rectified sine is carried out with the following approach: To reproduce an order of magnitude in $u(t)$ (fig. 2(b)), about three harmonics are necessary, for two orders of magnitude ten harmonics, respectively. Accordingly, the pulse train is reconstructed with about seven harmonics for an order of magnitude of $u(t)$, and with about seventeen harmonics for two orders of magnitude. The pulse train reveals clearly that a high amount of frequencies must be resolved to reconstruct a time signal. The half-wave rectified sine and pulse train shaped jet velocity has the analytically inverse discrete Fourier-Transform of

$$\text{half-wave rectified sine}: \quad IDFT(u_{\text{jet}}(t)) = \frac{\hat{u}}{\pi} + \frac{\hat{u}}{2}\sin(\omega_0 t) + \frac{2\hat{u}}{\pi}\sum_{n=2,4,6,\ldots}^{\infty} \frac{\cos(n\omega_0 t)}{n^2 - 1}, \tag{20}$$

$$\text{pulse train}: \quad IDFT(u_{\text{jet}}(t)) = \frac{\hat{u}}{2} + \sum_{n=1}^{\infty}\left[\frac{2\hat{u}}{n\pi}\sin(\frac{n\pi}{2})\right]\cos(n\omega_0 t), \quad DC = 0.5. \tag{21}$$

Both Eqs. (20) and (21) have a zero frequency component equivalent to a mean value, which is $\hat{u}/\pi$ for the half-wave rectified sine excitation and $\hat{u}/2$ for the pulse train with a duty cycle of 0.5. Eq. (20) signifies the influence of even multiples of the fundamental frequency only for the half-wave rectified sine, and these multiples decay with $1/n^2$. The pulse train, Eq. (21), is influenced by odd multiples of the fundamental frequency only, and these multiples decay with $1/n$ only. Therefore, fluidic actuators with pulsating jet velocities have a wide frequency range with which the flow can be influenced.

The basis for the applicability of LFD to AFC is the accurate prediction of dynamic response data with a harmonic shaped jet velocity actuation. The enormous dependence of pulsating jet velocities on higher harmonics also raises the question to what extent a linearized method can still be used efficiently, given that each harmonic is calculated sequentially.

Fluidic actuation is often characterized with the blowing momentum coefficient expressing the relationship between the jet momentum and the dynamic pressure force. The blowing momentum coefficient was first introduced by Poisson-Quinton[46] and for this application is defined as

$$C_\mu = \frac{DC\,\dot{m}_{\text{jet}}u_{\text{jet}}}{\frac{1}{2}\rho_\infty U_\infty^2 S_{\text{ref}}}, \quad \rho_{\text{jet}} \approx \rho_\infty: \quad C_\mu(\%) = 2DC\frac{S_{\text{jet}}}{S_{\text{ref}}}\left(\frac{u_{\text{jet}}}{U_\infty}\right)^2 \times 100, \tag{22}$$

being DC the actuation duty cycle, $\dot{m}$ the time-averaged actuation mass-flow, and u_{jet} is the time-averaged jet velocity. It further contains free-stream values of the density (ρ_∞) and velocity (U_∞), and S_{ref} is the airfoil reference area and S_{jet} is the slot area.

American Institute of Aeronautics and Astronautics

IV. Results

IV.A. NACA4412 with single slot

The computational setup consists of the NACA 4412 non-symmetrical airfoil with a high maximum camber thickness of 4 % reaching the maximum camber thickness at 40 % of the cord length. It is a typical airfoil for low speed and is suitable to high angles of attack to study viscous flow, Ref.[47, 48] Most fluidic actuation applications on airfoils at low speed consider the control of lift, and thus, the validations and results contain only this coefficient. The drag and pitching moment coefficient can also be determined simultaneously.

Table 1. Flow conditions for the baseline NACA 4412 airfoil.

$\bar{\alpha}$ [deg]	U_∞ [m s^{-1}]	T_∞ [K]	p_∞ [Pa]	Re$_\infty$ [-]	$l_{\text{ref}} = c$ [-]
0	92.6	288	101 325	6.3×10^6	1

Table 1 lists the flow conditions, which are set to $U_\infty = 92.6$ m s^{-1} at wind tunnel conditions of 101 325 Pa and an ambient temperature of 288 K, resulting in a Reynolds number of about 6.3×10^6. Mainly two cases, the baseline at $\alpha = 0$ deg and a higher $\alpha = 12$ deg, are considered for investigating both the amplitude-response function (ARF) and the frequency response function (FRF) of the global load coefficients. An intermediate case at $\alpha = 6$ deg is included for certain validations as well.

Table 2. Considered cases for the NACA 4412 for constant blowing of $\bar{u} = 50$ m s^{-1}, $C_\mu = 0.117\%$.

Case	$\bar{\alpha}$ [deg]	$\hat{u}$[m s^{-1}]	f [Hz]
Stead-state static derivatives			
baseline, intermediate, higher $\bar{\alpha}$	[**0**,3,**6**,9,10,11,**12**]	10-90[a]	0
Sine wave			
baseline, FRF	0.0	1	0.1-300[b]
baseline, FRF and ARF	0.0	1/12.5/25/50	0.1-300[b]
derivative, higher $\bar{\alpha}$	12.0	1	0.1-300[b]
Half-wave rectified sine			
baseline	0.0	1	75
derivative, higher $\bar{\alpha}$	12.0	1	75
derivative, $\bar{\alpha}$, ARF	0	1-50[c]	75
Pulse train			
baseline	0.0	1	75
derivative, higher $\bar{\alpha}$	12.0	1	75

[a] incremental, 9 instances together

[b] incremental, 16 instances together

[c] incremental, 4 instances together

Table 2 summarizes the computed cases for the NACA 4412 airfoil based on a constant blowing jet velocity of 50 m s^{-1}. The reasons for the validation with a nonzero mean actuation jet velocity is related to the slot modeling. A well developed flow in the slot is of great advantage for validations with a small jet excitation, since a velocity of zero easily forms vortices in the slot that affects the numerical behavior of the boundary condition. The flux-based boundary condition has the unpleasant property of swaying back and forth between suction and blowing at very low speeds and can prevent the convergence of the steady-state simulation, which make validation more difficult. Steady-state static derivatives for the lift coefficient are evaluated for seven angles of attack and a mean actuation jet velocity between 10 and 90 m s^{-1}. Fluidic actuation is performed with a constant, sinusoidal and pulsed blowing (half-wave rectified sine and pulse train). Frequency response and amplitude response functions are simulated for about three orders of magnitude in frequency and for four different amplitudes in the excitation jet velocity for cases $\bar{\alpha} = 0$ and $\bar{\alpha} = 12$ deg. The same α cases

American Institute of Aeronautics and Astronautics

have been chosen for reconstructing the impulse response of the lift coefficient for the half-wave rectified sine and pulse train excitation jet velocities.

(a) NACA 4412 airfoil

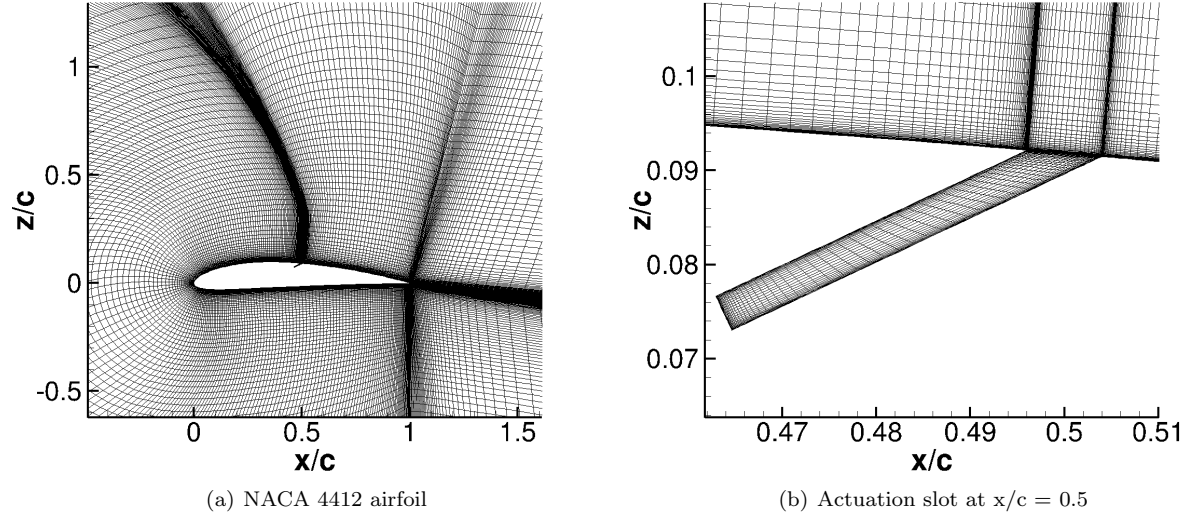(b) Actuation slot at x/c = 0.5

Figure 3. Nearfield computational grid (a) and actuation slot (b) for the NACA 4412 case.

Figure 3(a) shows the near body resolution of the structured computational grid around the NACA 4412 airfoil. This grid around the NACA 4412 airfoil with a bluff trailing edge consists of 57 666 grid nodes and is a typical C-type grid, where the farfield is set to a maximum dimension of $60 \times c$. With a chord length of $c = 1$, the slot in fig. 3(b) is located at $x/c = 0.5$ on the upper side of the airfoil and it is inclined downstream by 25 degrees. The slot width measures $0.004c$ and the length is $0.04c$. Steady-state flow (RANS) simulations were performed for different constant blowing and for various angles of attack. The applied solution technique is a full approximation storage acceleration technique, which is a 4 level W-cycle geometrical multigrid, Ref.[27] All RANS simulations are converged to machine accuracy, that is 14 orders of magnitude for the density residual. This strict termination criterion ensures the initial condition for the LFD method ($\mathbf{R} \approx 0$).
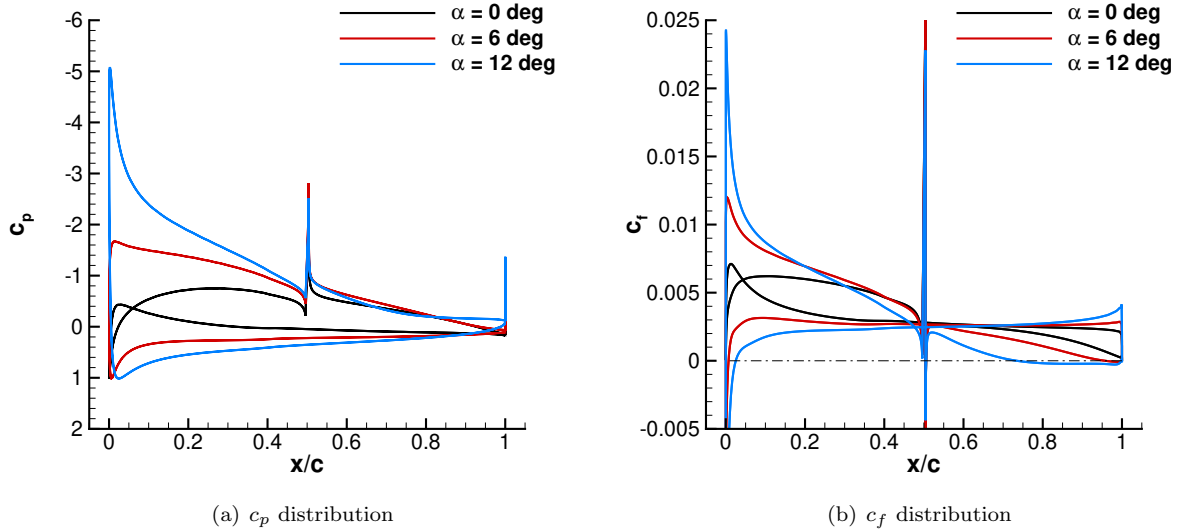

(a) c_p distribution

(b) c_f distribution

Figure 4. RANS-obtained (a) surface pressure and (b) skin friction coefficient distribution for the NACA 4412 case, $U_\infty = 92.6 \, \mathrm{m \, s^{-1}}$, $\mathbf{Re}_\infty = 6.34 \times 10^6$, $\alpha = 0/6/12 \, \mathrm{deg}$, $\bar{u} = 50 \, \mathrm{m \, s^{-1}}$.

Figure 4 shows the surface pressure and skin friction coefficient for three distinct angles of attack, $\alpha = 0/6/12 \, \mathrm{deg}$ for a constant blowing jet velocity of $50 \, \mathrm{m \, s^{-1}}$. The c_p as well as the c_f distribution in figs. 4(a)

American Institute of Aeronautics and Astronautics

and 4(b) at the actuation slot location, $x/c = 0.5$, on the upper side of the airfoil exhibits a strong peak. Resulting from this strong influence of the actuation boundary condition on the c_p and c_f distributions, this boundary condition is neglected for the evaluation of forces and moments on the airfoil. Figure 4(b) indicates the first separation on the upper side of the airfoil near the trailing edge at $\alpha = 6$ deg. The flow on the upper side is separated in the case $\alpha = 12$ deg from the trailing edge upstream to about 75 % of the cord length. Based on these results, the investigation of the ARF and FRF includes the attached flow case at $\alpha = 0$ deg and a detached flow case at $\alpha = 12$ deg.

Table 3. Computational parameters employed in the LFD and URANS simulation of the NACA 4412 cases.

Parameter	Value
LFD	
minimum residual abort criterion (absolute)	10^{-10}
Krylov-GMRES iterations	50
ILU, 2nd order preconditioning weight	0.5
CFL number (fine)	40/-
URANS	
minimum residual abort criterion	1×10^{-7}
physical time-steps per period	100
maximum pseudotime iterations	500
multigrid cycle (level-type)	4W-sym
Number of periods	10
CFL number (fine/coarse grid)	40/40

Table 3 summarizes the computational parameters of the URANS and LFD simulations. Convergence for the LFD method was reached throughout by aborting at a minimum residual of 1×10^{-10}. URANS simulations are strongly subject to user experience, with slightly modified parameters leading to varying CPU-times. Particularly, the CPU-time reduction factor between URANS and LFD can become skewed. An abort criterion of 1×10^{-7} for the inner loop convergence for the dual-time stepping approach for the URANS calculations was set to sufficiently converge the flow variables and the turbulent transport variable for attached and detached flow conditions. URANS simulations need an extensive search for the correct number of time steps per period and number of periods, since the transient phase requires considerable time by applying fluidic actuation. As investigasted by Ciobaca et. al.,[12] 100 time steps per period have been selected with a total of ten periods, which satisfies a trade-off to guarantee well converged air load coefficients as well as efficient simulation times.

For constant blowing ($\bar{u} > 0$), the derivative of air loads can be calculated with respect to changes in the mean jet velocity. These derivatives are commonly referred as steady-state static derivatives. Figure 5 shows steady-state static derivatives of the lift coefficient versus the mean jet velocity and versus angle of attack variation. In the nonlinear case for RANS simulations, a finite differencing (FD) is applied with a steps size of $\epsilon = \pm 0.1 \, \text{m s}^{-1}$ to the mean jet velocity. The LFD resolves static derivatives by setting $f = 0$. Both figs. 5(a) and 5(b) reveal a lift gain for positive C_L derivatives, and a lift reduction for negative C_L derivatives. In fig. 5(a), the sign switch appears from being negative to positive for the lower $\alpha = 0/6$ deg cases around $\bar{u} = 60 \, \text{m s}^{-1}$. Both C_L derivatives for the lower α cases indicate a shallow change over mean actuation velocity. For case $\alpha = 12$ deg, the switch between negative and positive C_L derivative is shifted to a lower mean jet velocity of about $50 \, \text{m s}^{-1}$, and the distribution shows an increased sensitivity to the actuation velocity whenever large areas of flow separation are present. Figure 5(b) depicts for the lower $\bar{u}_{\text{jet}} = 30 \, \text{m s}^{-1}$ an increasing lift reduction and for the higher $\bar{u}_{\text{jet}} = 70 \, \text{m s}^{-1}$ an increasing lift gain with increasing angle of attack. The middle case for $\bar{u}_{\text{jet}} = 50 \, \text{m s}^{-1}$ presents a different behavior in comparison to the other two cases. A moderate, almost linear, lift reduction is encountered from the lowest α to about nine degrees, where it reaches its maximum lift reduction. Above $\alpha = 9$ deg, the lift reduction reduces rapidly and reaches nearly zero at $\alpha = 12$ deg.

The first investigation regarding dynamic derivatives is performed for the behavior of the first harmonic of the lift coefficient for various sinusoidal actuation velocities ($\hat{u}$) versus frequency. The first harmonic of

(a) $\alpha = 0/6/12\,\mathrm{deg}$ **(b)** $\bar{u}_{\mathrm{jet}} = 30/50/70\,\mathrm{m\,s}^{-1}$
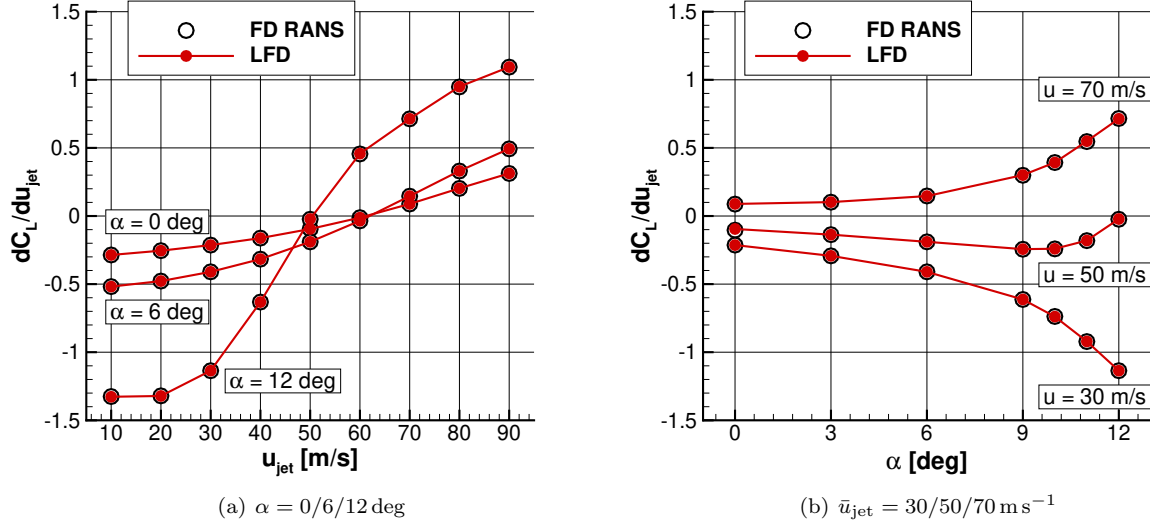
Figure 5. Steady-state static derivatives of C_L versus mean jet velocity (a), and versus angle of attack (b) for different constant blowing jet velocities for the NACA 4412 case obtained with central finite differencing of RANS (FD RANS) solutions and the LFD method.

the C_L magnitude is presented in a frequency (FRF) and amplitude response function (ARF) obtained with URANS simulations.

Figures 6(a) and 6(c) shows the URANS-obtained ARF and FRF of the first harmonic magnitude of C_L for sinusoidal excitation of the actuation jet velocity with a constant blowing of $\bar{u} = 50\,\mathrm{m\,s}^{-1}$. Two angles of attack ($\alpha = 0/12\,\mathrm{deg}$) are considered for a frequency band between 1-300 Hz and magnitudes of actuation jet velocities of $\hat{u} = \mathbf{0.5}/12.5/25/\mathbf{50}\,\mathrm{m\,s}^{-1}$ for the subsonic flow past the NACA 4412 airfoil. The magnitude of the fluctuating actuation jet velocity of $\hat{u} = 50\,\mathrm{m\,s}^{-1}$ with a constant blowing of $\bar{u} = 50\,\mathrm{m\,s}^{-1}$ marks the case, where the blowing jet velocity reaches zero during one period at $t/T = 3T/4$, see fig. 2(a). The ARFs for an excitation frequency of 75 Hz in figs. 6(b) and 6(d) include the results of the LFD method. The attached flow of the baseline case at $\alpha = 0\,\mathrm{deg}$, (fig. 6(a)), reveals a decrease in dynamic response with increasing blowing excitation magnitudes. Note that the low frequency asymptotes reach the steady-state static derivatives, see fig. 5. The FRF distributions for each $\hat{u}$ over the frequency are almost equal in shape with a decreasing offset between the excitation magnitudes at the upper end of the frequency band. The dynamic transfer behavior of $\hat{u}$ to the magnitude of the first harmonic of lift encloses a minimum at about 30 Hz, which then rises steeply until about 100 Hz continued with a moderate drop at the highest frequencies. Figure 6(d) shows the LFD/URANS-obtained ARF of the lift magnitude versus excitation jet velocity for an excitation frequency of 75 Hz. The LFD result is constant, which satisfies the assumption for being dynamically linear over $\hat{u}$. Its URANS counterpart becomes dynamically nonlinear above $\hat{u} \approx 10\,\mathrm{m\,s}^{-1}$. Yet, the drop in the magnitude of C_L is moderate to about 20 % of the LFD result for the highest $\hat{u}$.

Figure 6(c) presents the FRF for various excitation jet velocities for the detached NACA 4412 airfoil case at $\alpha = 12\,\mathrm{deg}$. Also for this case, the dynamic response decreases over the frequency with increasing excitation jet velocity, except for the low frequency asymptotes ($f < 3\,\mathrm{Hz}$). For the attached case at $\alpha = 0\,\mathrm{deg}$, (fig. 6(a)), the low frequency asymptotes decrease with increasing excitation magnitude which conforms to the overall distribution. This behavior is reverted for the detached case in fig. 6(c) for frequencies below 3 Hz. The low frequency asymptotes increase with increasing excitation magnitude and points out the nonlinear behavior with such excitation magnitudes for detached flow cases. The dependence on the excitation jet velocity is more distinctive between the individual FRFs, but the shape of the distributions is almost the same, and approach each other at higher frequencies. Similar to the attached flow case (fig. 6(a)), the FRFs become less sensitive for the magnitude of the excitation jet velocities with frequencies above 100 Hz. The local minimum of the C_L magnitude is shifted to about 40 Hz for all FRFs, followed by an intense rise reaching the same local maximum as the attached flow case at about 100 Hz. Above 100 Hz, the FRFs drop suddenly with an intermediate local maximum at about 160 Hz. Regardless of the excitation jet velocity and for that particular flow conditions, both cases reach the maximum dynamic response at an
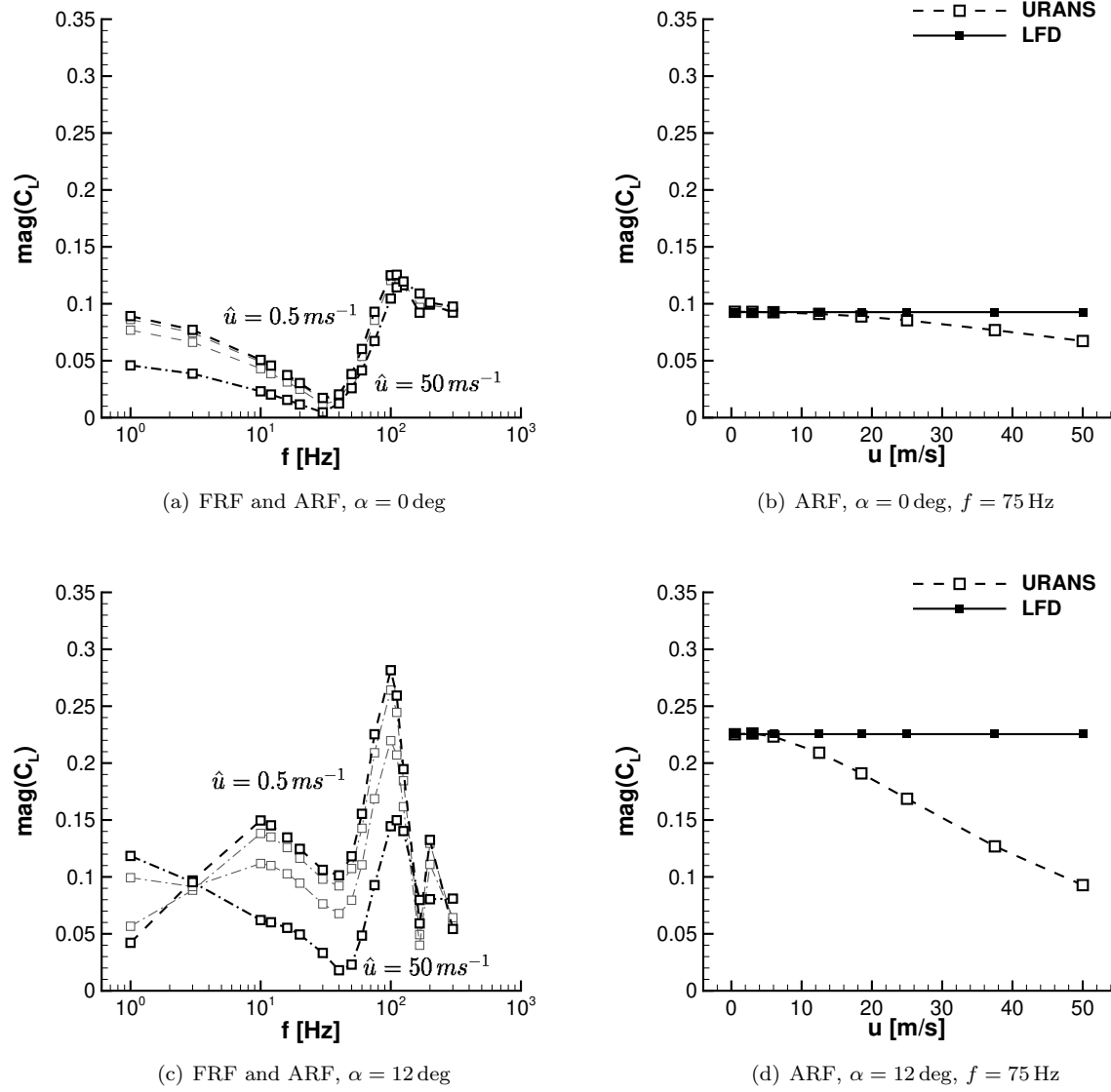
(a) FRF and ARF, $\alpha = 0 \deg$

(b) ARF, $\alpha = 0 \deg$, $f = 75\,\mathrm{Hz}$

(c) FRF and ARF, $\alpha = 12 \deg$

(d) ARF, $\alpha = 12 \deg$, $f = 75\,\mathrm{Hz}$

Figure 6. Obtained URANS FRF ((a), (c)) for jet excitation magnitudes of $\hat{u} = 0.5/12.5/25/50\,\mathrm{m\,s}^{-1}$, and ARF for $f = 75\,\mathrm{Hz}$ ((b),(d)) for the first harmonic magnitude of C_L with sinusoidal jet excitation for the NACA 4412 at $\alpha = 0 \deg$ (top) and $\alpha = 12 \deg$ (bottom), $U_\infty = 92.6\,\mathrm{m\,s}^{-1}, \bar{u} = 50\,\mathrm{m\,s}^{-1}$.

excitation frequency of 100 Hz. The high dependence on the excitation jet velocity is also illustrated for the ARF in fig. 6(d) for $f = 75$ Hz. Dynamically nonlinear behavior is already present for an excitation jet velocity of 5 to $6\,\mathrm{m\,s}^{-1}$, and drops to about half the magnitude of the LFD result for the highest $\hat{u}$. Thus, linear scaling of the magnitude of C_L is possible for a certain range of $\hat{u}$ for attached flow conditions, but it becomes almost impracticable for the detached flow conditions.

Figure 7 shows the polar plots for the first harmonic of C_L for a constant blowing of $50\,\mathrm{m\,s}^{-1}$ with a sinusoidal excitation magnitude of $0.5\,\mathrm{m\,s}^{-1}$ in comparison with URANS and LFD results. Figures 7(a) and 7(b) present a remarkable consistency between both numerical methods over the investigated frequency range. Important is the switch between phase lead and phase lag: For the case $\alpha = 0 \deg$ (fig. 7(a)), a phase lag appears for the lowest frequencies to about $f = 40$ Hz, then between $f = 40 - 270$ Hz there is a phase lead, and above $f = 270$ Hz it shifts to a phase lag again. A phase lead of a transfer function for actuation has the advantage, that the lift response is instantly with regard to its input excitation. Contrarily, a phase lag decreases the transfer speed allowing for a damping of low and high frequencies. The magnified detail in fig. 7(a) discovers a loop of the C_L response between 145-195 Hz with a local minimum at 167 Hz. It
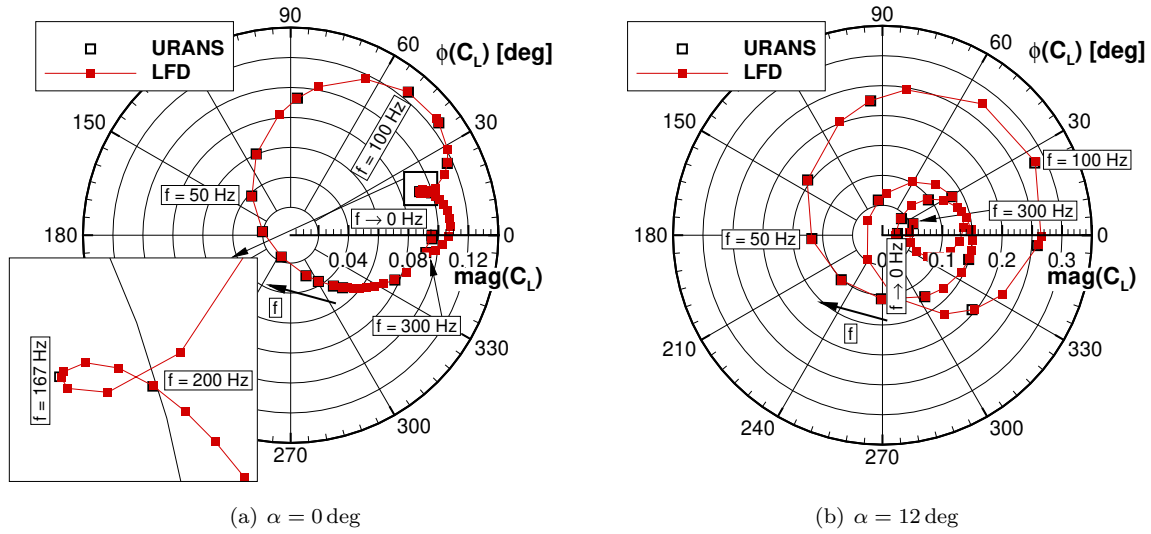
American Institute of Aeronautics and Astronautics

(a) $\alpha = 0 \deg$ (b) $\alpha = 12 \deg$

Figure 7. Polar plot of FRF of LFD/URANS-obtained of the first harmonic of C_L for the NACA 4412 with sine excitation, $U_\infty = 92.6\,\mathrm{m\,s^{-1}}, \bar{u} = 50\,\mathrm{m\,s^{-1}}, \hat{u} = 0.5\,\mathrm{m\,s^{-1}}$ for both $\alpha = 0/12\deg$ cases.

indicates the same C_L response for frequencies of 145 and 195 Hz. Figure 7(a) contains further important information for the reconstruction of time signals. Is the fundamental frequency in the range with the smallest magnitude at about 30-40 Hz, the first three to four multiple harmonics (nf_0, $n = 1, 2, 3, \ldots$) are in the frequency range with the largest magnitude. It can thus be assumed that the time response is strongly influenced by higher harmonic components. Whenever the fundamental frequency is in the frequency range with the largest magnitude at approximately 75 - 125 Hz, the higher multiple harmonics are much smaller in magnitude, and the lift response will remain mainly first harmonic dominant.

The helical lift response for the detached flow case in fig. 7(b) starts at 0 Hz with a phase shift of 0 degrees with the first local minimum of the magnitude at about 40-50 Hz, and steadily increases to about 100 Hz. Thereafter, the response drops steadily with a zero crossing of the phase at about 110 Hz. A second zero crossing of the phase is at 225 Hz. Also for that case, higher harmonics of frequencies above 110 Hz have a small influence on the time response of the lift. In comparison with the attached flow case, the first local minima and maxima are slightly shifted to higher frequencies.

These sinusoidal oscillations can now be used to reconstruct time signals of air loads. A number of multiple harmonics are sequentially calculated with the LFD and then superposed (Eq. (18)) to form the final time response. The first investigative step is the study of the impulse response of the lift coefficient with respect to excitation frequency obtained from URANS simulations.
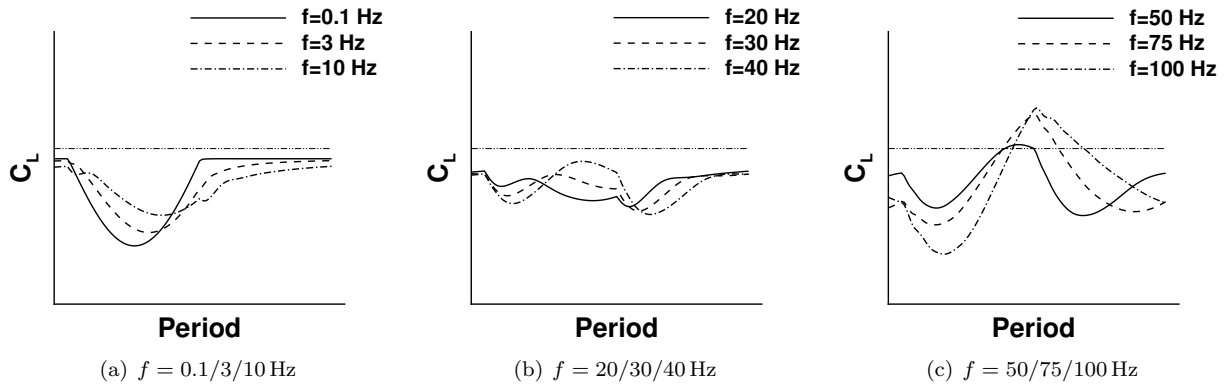

(a) $f = 0.1/3/10\,\mathrm{Hz}$ (b) $f = 20/30/40\,\mathrm{Hz}$ (c) $f = 50/75/100\,\mathrm{Hz}$

Figure 8. Evolution of the time response of C_L for one period versus excitation frequency for the NACA 4412 for $\alpha = 0\deg, \bar{u} = 50\,\mathrm{m\,s^{-1}}, \hat{u} = 1\,\mathrm{m\,s^{-1}}$ applying a half-wave rectified sine actuation jet velocity including the RANS mean value as reference.

American Institute of Aeronautics and Astronautics

Figure 8 depicts the evolution of the time response for one period for the lift coefficient with increasing excitation frequency for the NACA 4412 applying a blowing half-wave rectified sine actuation jet velocity on top of a constant blowing of $50\,\mathrm{m\,s^{-1}}$. The mean value of C_L obtained from the RANS simulation is included in all figures. Blowing actuation with half-wave rectified sine jet velocities yields a decrease in lift, since all actuation mean values of C_L are below the RANS mean value. The first fig. 8(a) presents the lift coefficients time response for the lowest frequencies, and for $0.1\,\mathrm{Hz}$ the actuation jet velocity signal shape is mainly preserved for the lift response. Excitation frequencies between 1-10 Hz downsize the time signal minimally, but blur the response at the discontinuity with increasing frequency. The mid-range excitation frequencies around 20-40 Hz, fig. 8(b), generate an irregular behavior on the time response. It is mainly flattened with the presence of higher harmonics. As explained before for fig. 7, the fundamental excitation frequency has its smallest influence, since its first harmonic magnitude reaches a minimum. The second to fourth harmonics are present, which coincides with the frequency range where the maximum magnitude of the lift coefficient response appears. Another reason is the interference of the actuation jet with the main flow. Exactly at these excitation frequencies the interaction with the main flow is activated and at its highest. Figure 8(c) contains an indication that the excitation frequencies of 75 and 100 Hz for the half-wave rectified sine actuation jet generate first harmonic dominant time responses with a low presence of higher harmonics. The peaks of the C_L time response appear at almost $T/2$, at the discontinuity of the actuation jet.
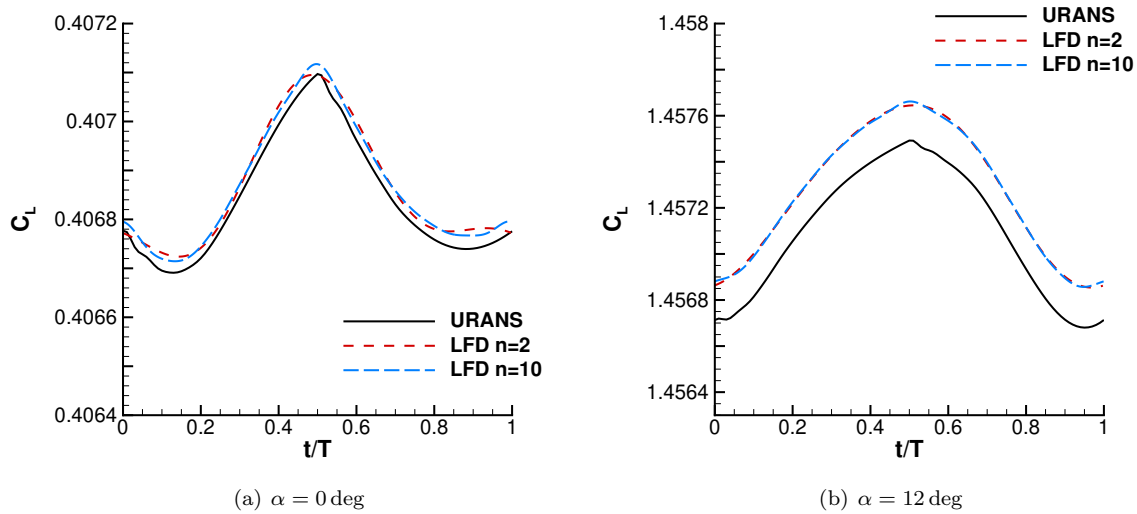

(a) $\alpha = 0\,\mathrm{deg}$ (b) $\alpha = 12\,\mathrm{deg}$

Figure 9. C_L **time response recovery for both** $\alpha = 0$ **(a) and** $\alpha = 12\,\mathrm{deg}$ **(a) cases for the NACA 4412 applying a blowing half-wave rectified sine actuation jet velocity,** $f = 75\,\mathrm{Hz}, \bar{u} = 50\,\mathrm{m\,s^{-1}}, \hat{u} = 1\,\mathrm{m\,s^{-1}}$.

In fig. 9, the recovery of the time response of the lift coefficient is performed with the LFD in comparison with URANS for an excitation $f = 75\,\mathrm{Hz}$ and a half-wave rectified actuation jet velocity with a magnitude of $\hat{u} = 1\,\mathrm{m\,s^{-1}}$ for $\alpha = 0/12\,\mathrm{deg}$. Two LFD results are included in both figs. 9(a) and 9(b), the recovery with the zero frequency component and two harmonics (n=2) as well as with ten harmonics (n=10). A good accuracy is achieved for the response representation with the LFD method by including a minimum of two harmonics in comparison with URANS. Deviations appear at the discontinuities of the actuation jet signal at $t/T = 0$ and at the signals peak $t/T = 0.5$ for $n = 2$, and almost entirely vanish by increasing the number of harmonics to $n = 10$ for the LFD method. A certain mean C_L offset between URANS and LFD method is visible in both figs. 9(a) and 9(b), which increases from the baseline $\alpha = 0\,\mathrm{deg}$ to $\alpha = 12\,\mathrm{deg}$. Fluidic actuation is applied with blowing only, and thus, the kinetic energy increases constantly over one period, $E_{\mathrm{kin}}(t) = 1/2|(\bar{u} + \tilde{u}(t))|^2$, and that changes the mean flow variables. This change of the mean flow variables is not captured by the RANS solution, the underlying steady-state solution for the LFD.

The evolution of the time response of C_L for various excitation frequencies over one period is shown in fig. 10 for the NACA 4412 applying a blowing pulse train actuation jet velocity on top of a constant blowing of $50\,\mathrm{m\,s^{-1}}$. All figs. 10(a) to 10(c) include the RANS mean value as a reference. This blowing actuation with pulse train jet velocities yields a higher decrease in lift compared with a half-wave rectified sine jet velocity noticeable in the mean value shift. It is directly related to the zero frequency component, which is $\hat{u}/2$ for the
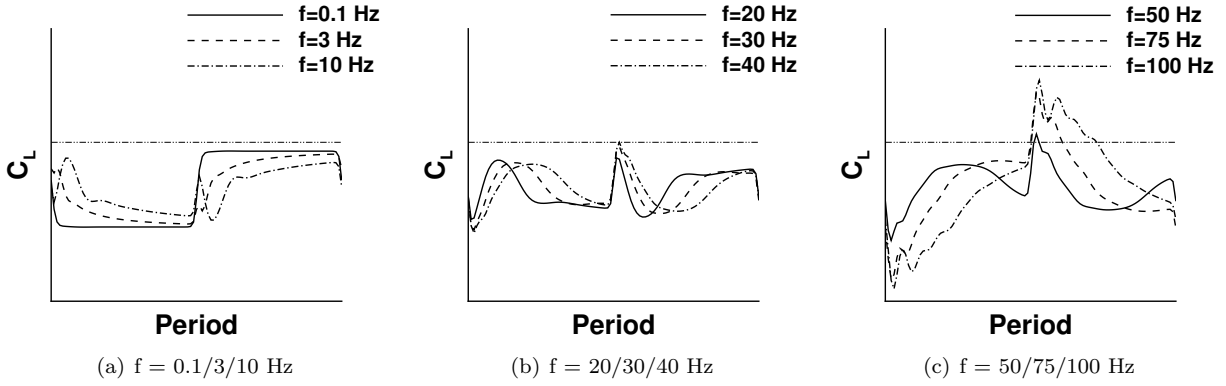
Figure 10. Evolution of the time response of C_L for one period versus excitation frequency for the NACA 4412 for $\alpha = 0\,\text{deg}, \bar{u} = 50\,\text{m}\,\text{s}^{-1}, \hat{u} = 1\,\text{m}\,\text{s}^{-1}$ applying a pulse train actuation jet velocity including the RANS mean value as reference.

pulse train and $\hat{u}/\pi$ for the half-wave rectified sine actuation. The lift coefficient response for the smallest excitation frequency of $0.1\,\text{Hz}$ in fig. 10(a) corresponds to the actuation jet velocity shape. With increasing excitation frequency, $f = 3 - 10\,\text{Hz}$, the magnitude of the C_L response slightly decreases and gets blurred at the discontinuity. For $f = 10\,\text{Hz}$, two distinctive overshoots appear near the discontinuities at $t = 0$ and $t = T/2$. Figure 10(b) shows again a flattening of the C_L response for the mid-range excitation frequencies. The ringing at each half period has intensified and expands to an increasing degree for almost half a period ($f = 40\,\text{Hz}$). Higher excitation frequencies in fig. 10(c) reveal an amplification of the C_L response. The shape of the time response is in the first half of the period likewise a bell curve, continued with an observable overshoot at $t = T/2$, and an almost linear decrease similar to a sawtooth. At the highest frequency of $f = 100\,\text{Hz}$, the C_L response has a increased tendency to oscillations shortly past $t = T/2$ caused by the presence of high frequencies.
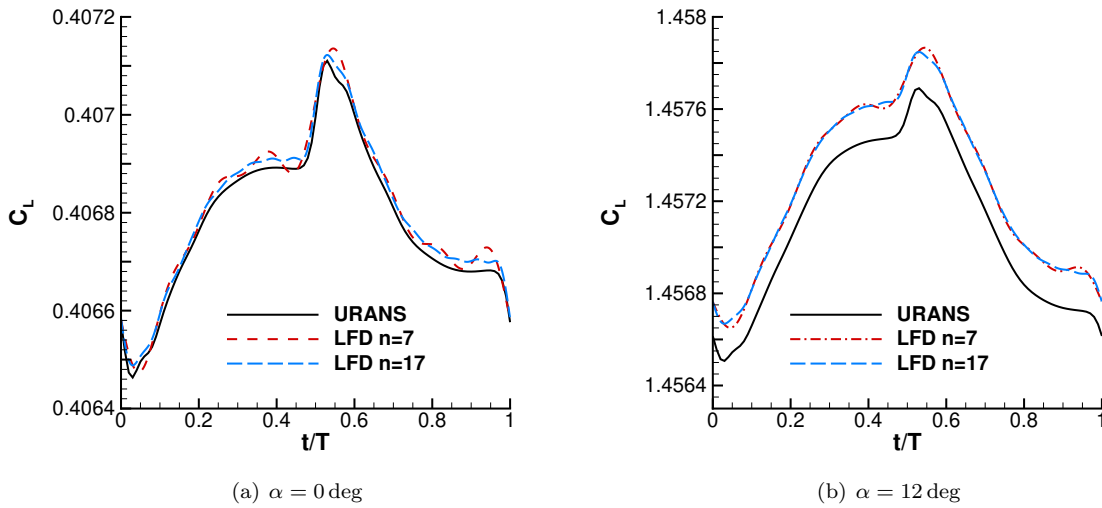

Figure 11. C_L time response recovery for both $\alpha = 0$ (a) and $\alpha = 12\,\text{deg}$ (b) cases for the NACA 4412 applying a blowing pulse train actuation jet velocity, $f = 75\,\text{Hz}, \bar{u} = 50\,\text{m}\,\text{s}^{-1}, \hat{u} = 1\,\text{m}\,\text{s}^{-1}$.

Figure 11 displays the recovery of the time response of the lift coefficient with the LFD method in comparison with URANS for a blowing pulse train excitation with a magnitude of $\bar{u} = 50\,\text{m}\,\text{s}^{-1}$ and $\hat{u} = 1\,\text{m}\,\text{s}^{-1}$ for $f = 75\,\text{Hz}$ and for two angles of attack $\alpha = 0/12\,\text{deg}$. Both figs. 11(a) to 11(b) include the LFD results with the zero frequency component with seven and seventeen harmonics. The LFD results with seven harmonics show small overshoots for both α cases. The general shape of the C_L response is well approximated with seven harmonics. The reconstruction of the time signal with seventeen harmonics is almost spot on to the URANS results, except for the mean value offset. For the $\alpha = 0\,\text{deg}$ case (fig. 11(a)) the mean offset

has nearly vanished, but for the $\alpha = 12\,\mathrm{deg}$ case, the mean offset is clearly visible. Particularly noticeably is the ringing at the discontinuities (Gibbs phenomenon), around $t/T = 0$ and $T/2$, which naturally decreases with the resolution of more harmonics in the time signal.
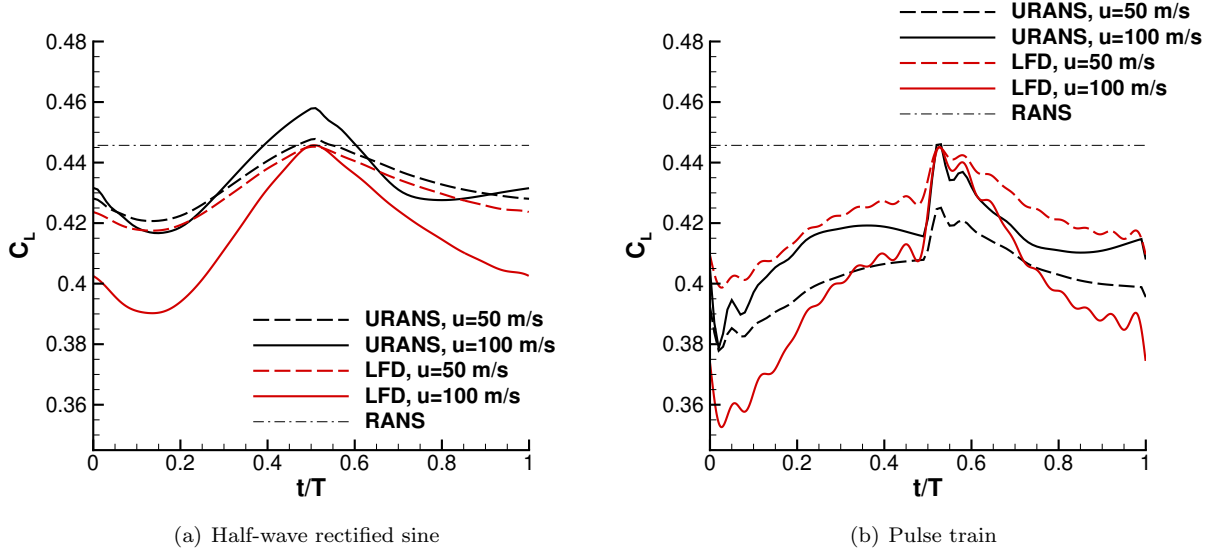

(a) Half-wave rectified sine (b) Pulse train

Figure 12. LFD/URANS-obtained time response of C_L for two different jet velocity magnitudes ($\hat{u} = 50/100\,\mathrm{m\,s^{-1}}$) for the (a) half-wave rectified sine and (b) pulse train for the NACA 4412 with an excitation frequency of $75\,\mathrm{Hz}$, $U_\infty = 92.6\,\mathrm{m\,s^{-1}}, \bar{u} = 0\,\mathrm{m\,s^{-1}}, \bar{\alpha} = 0\,\mathrm{deg}$.

Figure 12 shows the magnitude dependency on the time history for one period of C_L for an excitation frequency of $75\,\mathrm{Hz}$ based on $\bar{u} = 0\,\mathrm{m\,s^{-1}}$ for the NACA 4412 airfoil at $\alpha = 0\,\mathrm{deg}$ obtained with LFD and URANS simulations. Two different magnitudes of realistic actuation jet velocities, $\hat{u} = 50/100\,\mathrm{m\,s^{-1}}$, are chosen for the half-wave rectified sine (fig. 12(a)) and pulse train (fig. 12(b)) actuation jet velocity. Both figures include the mean value of C_L derived from the RANS computation as a reference. Each result of the rectified sine half-wave actuation in fig. 12(a) are similar to a certain degree for that excitation frequency, see also fig. 9(a). The linear scaling in magnitude of the time response for the smaller actuation magnitude is well resolved, but for very high actuation jet magnitudes, it will introduce accuracy losses (see also ARF in fig. 6(b)). The peaks of the LFD results at $t/T = 0.5$, which are the maximum values, are exactly on the RANS mean value, and that relation is given by applying Eq. (18). There are no overshoots in both time responses that indicate the Gibbs phenomenon at the time instances near $t/T = 0$ and $t/T = 0.5$. Both time responses are smooth. URANS results show an offset of the RANS mean value, since both peaks have different maximum values at $t/T = 0.5$, and this offset is related to a lift gain or reduction which is introduced by the energy impulse of the actuation jet. The change of the mean value over excitation magnitude and excitation frequency cannot be modeled with the LFD approach. Figure 12(b) includes the C_L responses for the same magnitudes of a pulse train excitation. Again, the shape of the response can be well captured even with the characteristic peak near $t/T = T/2$ for that excitation frequency. An accuracy loss is eminent for a linear scaling of the response for excitation magnitudes above $50\,\mathrm{m\,s^{-1}}$. Contrarily to the half-wave rectified sine actuation, the pulse train actuation indicates the Gibbs phenomenon near the time instances of $t/T = 0$ and $t/T = 0.5$. The URANS results show the expected overshoots past the time instances of the discontinuity, while these overshoots occur for the LFD results before and past those time instances from the fifth harmonic onward.

IV.B.   DLR-F15 high-lift wing section

The DLR-F15 wind tunnel model is a two-dimensional wall-to-wall high lift model investigated by Wild.[49] The setup considered for flow control is a two-element configuration that features a clean leading edge and a single-slotted flap.

Table 4 lists the subsonic flow conditions and geometrical properties of the DLR-F15 wing section in wind tunnel conditions. The subsonic viscous flow past the DLR-F15 is set to a free-stream Mach number

Table 4. Flow conditions for the DLR-F15 high-lift wing section.

$\bar{\alpha}$ [deg]	M_∞	T_∞ [K]	p_∞ [Pa]	Re_∞ [-]	$l_{\text{ref}} = c$ [-]	c_F
3	0.15	293	101 325	2×10^6	0.6	28 %c

of 0.15 and a Reynolds number of 2×10^6 million with an angle of attack of three degrees. It has a main chord length of 0.6 m with a flap chord length of 28 % of the main chord length.

(a) DLR F15 high-lift wing section
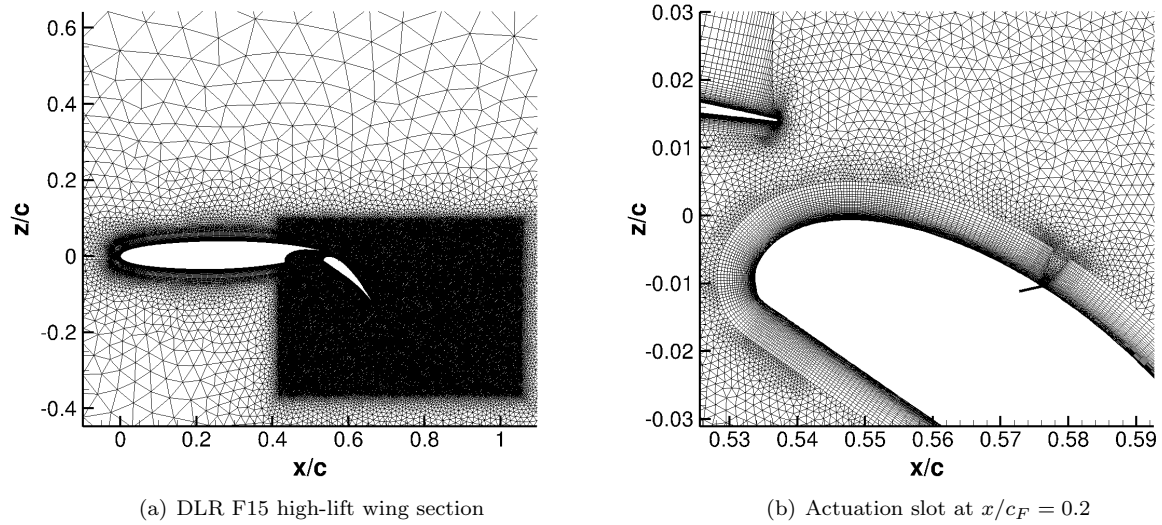
(b) Actuation slot at $x/c_F = 0.2$

Figure 13. Nearfield computational grid (a) and actuation slot (b) for the DLR F15 wing section.

Figure 13(a) shows the near body resolution of the computation grid for the DLR-F15 wing section which consist of about 377 000 grid nodes. The flap has a large deflection angle of 40 degrees. An additional refined block is placed around the flap to resolve the flow effects of fluidic actuation downstream of the flap. The single-slotted fluidic actuator in fig. 13(b) is inclined downstream by 45 degrees and located at $x/c_F = 0.2$ of the flap chord length with a constant width of 0.05 % of the main chord length. Actuation was performed to suppress the flow separation on the trailing-edge flap with a blowing pulse train actuation of $C_\mu = 0.225$ % ($\bar{u} = 0\,\text{m s}^{-1}, \hat{u} = 157\,\text{m s}^{-1}$) and an excitation period of 0.01 s ($f = 100$ Hz) with a duty cycle of 0.5.
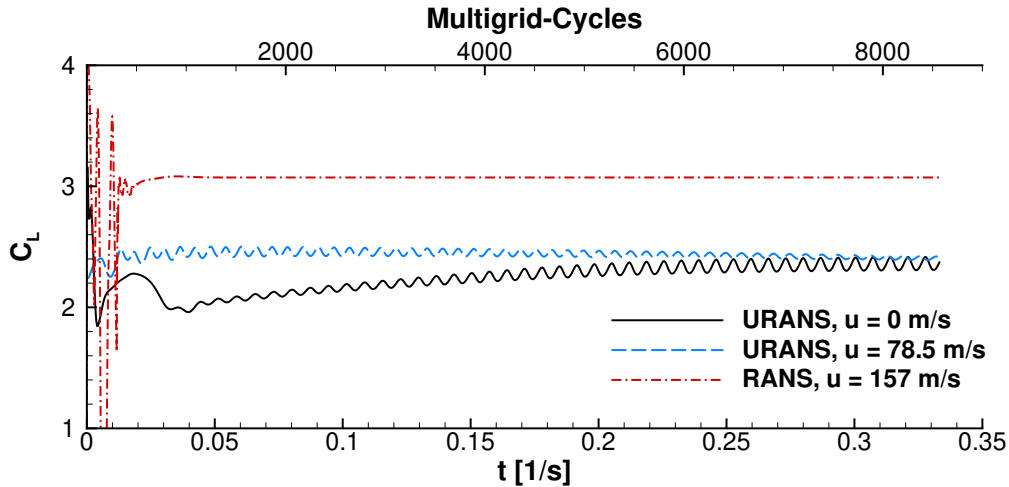

Figure 14. Convergence and time history of lift coefficient with constant blowing at $\bar{u} = 0\,\text{m s}^{-1}$, $\bar{u} = 78.5\,\text{m s}^{-1}$ and $\bar{u} = 157\,\text{m s}^{-1}$ for the DLR F15 case.

The initial experimental setup was designed so there was a flow separation at the trailing-edge of the flap. However, an approach using the existing LFD method is only possible with an initial steady-state RANS simulation. There are several ways to get a steady-state solution. Using another, more dissipative, numerical method or the use of a more dissipative turbulence model is currently not possible because of the missing linearization of such a scheme. Another approach is to increase the blowing jet velocity until a steady state is established. Figure 14 shows the convergence and time history with three differently constant blowing jet magnitudes of $\bar{u} = 0\,\mathrm{m\,s^{-1}}$, $78.5\,\mathrm{m\,s^{-1}}$ and $157\,\mathrm{m\,s^{-1}}$ to obtain an initial steady-state RANS solution for the DLR-F15. The former two URANS simulations were performed with a time step size of $0.000\,33\,\mathrm{s}$ for a total of $0.33\,\mathrm{s}$ resulting in $10\,000$ physical time steps. A steady-state simulation was achieved with the maximum blowing actuation jet magnitude, which serves as the basis for the following computation of the frequency response function with the LFD method. This test case is not subject to an in depth investigation of physical properties with the LFD, but it serves as the basis for measuring the computational efficiency. For more analysis on the physical behavior, the reader is advised to review Ciobaca et al.[11]
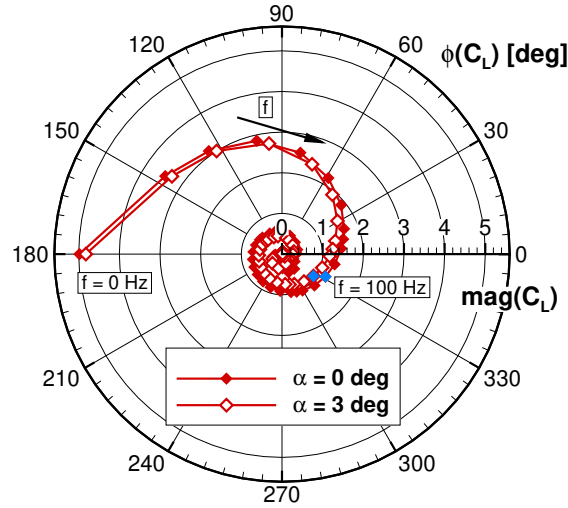

Figure 15. Polar plot of LFD-obtained FRF for constant blowing of $\bar{u} = 157\,\mathrm{m\,s^{-1}}$ with a sinusoidal actuation jet perturbation of $\hat{u} = 0.5\,\mathrm{m\,s^{-1}}$ for the DLR-F15 at $\alpha = 0\,\mathrm{deg}$ and $\alpha = 3\,\mathrm{deg}$, URANS-obtained values are in blue for $f = 100\,\mathrm{Hz}$.

Figure 15 depicts the LFD-obtained FRF in a polar plot for the baseline DLR-F15 at $\alpha = 3\,\mathrm{deg}$ and for a lower $\alpha = 0\,\mathrm{deg}$ for sinusoidal actuation jet excitation. The simulation of the FRF comprises a total of 134 frequencies in the range of $f = 0 - 2500\,\mathrm{Hz}$. Two additional computations are performed with URANS, marked as blue diamonds, which serve as a reference for the accuracy of the LFD results. Both helical FRFs are almost inherent of the angle of attack, starting with the maximum magnitude at $f = 0\,\mathrm{Hz}$, with a continuous decreasing in magnitude until reaching the maximum frequency. Regarding pulsed actuation, where such sinusoidal excitations of the actuation jet velocities are superposed to form the final time signal, higher harmonics above $300\,\mathrm{Hz}$ have in this case only a negligible influence on the time signal.

IV.C.   Computational Efficiency

The key-benefit of a LFD solver is the commonly established efficiency gain in comparison to non-linear URANS simulations. During the validation process the required CPU-time was assessed to substantiate the realizable CPU-time reduction of LFD-TAU and its URANS counterpart.

Table 5 lists the CPU-times for selected URANS and LFD simulations as well as the derived CPU-time reduction factor. The URANS as well as the LFD method need an initial RANS solution, which is dropped in the time reduction factors. Both methods used the same well-converged RANS solution necessary for the LFD method, although the requirements for an initial RANS solution may differ for the URANS method. URANS simulations were performed with ten periods, which guarantee a sufficient transient phase. In addition, the number of utilized processors are given. The CPU times of the LFD and URANS simulations are scaled with the number of processors, assuming linear speed-up of parallelization. LFD simulations were

American Institute of Aeronautics and Astronautics

Table 5. Quantitative comparison on the computational effort involved with the URANS (10 periods) and LFD (ILU, GMRES, sg) simulation for the NACA 4412 case ($CB = 50\,\mathrm{m\,s^{-1}}, \alpha = 0\,\mathrm{deg}$) and high-lift configuration, as well as the derived CPU-time reduction factor ($\zeta_{CPU} := CPU\text{-}time\ URANS/CPU\text{-}time\ LFD$).

| Case | simulation CPU-time (min), URANS: 10 periods | | | |
	URANS	LFD	CPU's	ζ_{CPU}
NACA4412 - sine excitation				
$\alpha = 0\,\mathrm{deg}$, f= 75 Hz[a]	20317	3.3	24/1	10731
$\alpha = 0\,\mathrm{deg}$, FRF[b]	408117	49.6	24/1	8221
NACA4412, f= 75 Hz - half-wave rectified sine excitation				
$\alpha = 0\,\mathrm{deg}$, n= 2	20317	7.9	24/1	2571
$\alpha = 0\,\mathrm{deg}$, n= 10	20317	20.9	24/1	972
$\alpha = 12\,\mathrm{deg}$, n= 2	20317	9.1	24/1	2230
$\alpha = 12\,\mathrm{deg}$, n= 10	20317	22.8	24/1	891
NACA4412, f= 75 Hz - pulse train excitation				
$\alpha = 0\,\mathrm{deg}$, n= 7	20317	16.1	24/1	1262
$\alpha = 0\,\mathrm{deg}$, n= 17	20317	31.4	24/1	647
$\alpha = 12\,\mathrm{deg}$, n= 7	20317	18.0	24/1	1129
$\alpha = 12\,\mathrm{deg}$, n= 17	20317	33.3	24/1	610
DLR-F15, f= 100 Hz - pulse train excitation				
$\alpha = 3\,\mathrm{deg}$, n= 7	72061	422	24/3	171
$\alpha = 3\,\mathrm{deg}$, n= 17	72061	669	24/3	108

[a] fundamental frequency, n = 1

[b] 16 frequencies

performed entirely by using the Krylov-GMRES technique in combination with an Incomplete Lower-Upper (ILU) preconditioner utilizing a first and second order weighting of the flux Jacobian. The residual abort criterion was set to 10×10^{-10} for all LFD simulations. All cases were performed on an Intel Xeon CPU X5650 with 2.67 GHz and 12 MB cache size.

A single sinusoidal perturbation achieves a speed-up of about four order of magnitude for the NACA 4412 airfoil with a single slot. Almost four orders of magnitude in speed-up are gained for the complete simulation of a FRF ($f = 0 - 300\,\mathrm{Hz}$) with sixteen instances for sinusoidal excitation including the zero frequency component. This minor reduction is caused by the different computation times of the LFD method, since lower frequencies need more simulation time as higher frequencies. In contrast, URANS simulations have marginal differences in computational time; only the achieved minimum residual differs. Resolving more than one frequency for a single time response, for example for a half-wave rectified sine actuation, yields a speed-up of more than three orders of magnitude with two frequencies and about three orders of magnitude with ten frequencies. The LFDs robust solution technique pays off regarding simulation times, which are nearly inherent for the attached flow conditions ($\alpha = 0\,\mathrm{deg}$) and the detached flow ($\alpha = 12\,\mathrm{deg}$) case. Thus, the speed-up of the LFD method is mainly driven by the number of computed frequencies in comparison with a single URANS simulation. For resolving a pulse train actuation with seventeen frequencies with the LFD method still gains a speed-up of about two and a half orders of magnitude in comparison with its counterpart.

The speed-up changes noticeably for the DLR-F15 wing-section case with the LFD method as a parallel application. Implicit solution techniques, like the Krylov-GMRES with the ILU-preconditioner, do not scale well for massive parallel applications. However, a speed-up of about 200 is gained for simulating seven harmonics including the zero frequency component, and about two orders of magnitude for seventeen harmonics, respectively.

American Institute of Aeronautics and Astronautics

V. Conclusions

The presented frequency domain method (LFD) is capable of computing dynamic response data for global air loads for active flow control applications accurately and efficiently for small perturbations in the jet velocity. Also steady-state static derivatives modeled as a small perturbation for the constant blowing magnitude is resolved with a satisfying accuracy. These static derivatives are of great importance, since they appear as zero frequency components in the time response by applying pulsed actuation jets. Constant blowing over a longer time has many applications, and extends to flight control to support ailerons or non-movable speed brakes. Static derivatives are of enormous importance for optimizing the ultimate blowing rate for increased efficiency.

Pulsed actuation introduce discontinuous jet velocity distributions such as half-wave rectified sine or pulse train jet velocities, and the number of harmonics retained in the time response may easily exceed twenty or more to represent a detailed time signal of the air loads. It has been shown, that the time response for a half-wave rectified sine actuation can be well resolved with about ten harmonics, and the pulse train with about seventeen harmonics plus the zero frequency component. Small periodic pulsed fluidic actuation, which behaves dynamically linear, can be computed accurately with the linear collocation of several harmonics to represent the air loads behavior in the time domain. A good estimation of time responses for pulsed excitations for fundamental frequencies above 70 Hz can be recovered qualitatively well with only two or three harmonics. Concerning an attached and detached flow: An initially attached flow offers significantly fewer restrictions for the actuation jet velocity magnitude than a detached flow. In principle, a detached flow immediately results in a non-linear behavior regarding increasing the jet magnitude.

The LFD method computes periodic perturbations based on the underlying steady-state flow solution and therefore cannot calculate a time change of the mean state variables. For example, pulsed blowing increases the kinetic energy over time in the domain, and thus, changes the flow variables in time. Yet, the small perturbation approach of the LFD for determining dynamic response data can be integrated well in an uncertainty investigation and optimization. Uncertainty quantification often deals with a high amount of data acquisition, and the speed-up of about two orders of magnitude of the LFD compared to URANS is still favorable when calculating a high number of perturbation frequencies.

References

[1]Greenblatt, D. and Wygnanski, I. J., "The control of flow separation by periodic excitation," *Progress in Aerospace Sciences*, Vol. 36, No. 7, 2000, pp. 487–545. doi: 10.1016/S0376-0421(00)00008-7.

[2]Gross, A. and Fasel, H. F., "CFD for Investigating Active Flow Control," *4th Flow Control Conference, Seattle, WA, AIAA Paper 2008-4310*, 2008.

[3]Seifert, A., Darabi, A., and Wyganski, I., "Delay of airfoil stall by periodic excitation," *Journal of Aircraft*, Vol. 33, No. 4, 1996, pp. 691–698. doi: 10.2514/3.47003.

[4]Schatz, M. and Thiele, F., "Numerical Study of High-Lift Flow with Separation Control by Periodic Excitation," *AIAA Paper 2001-0296*, 2001.

[5]Duvigneau, R. and Visconneau, M., "Optimization of a synthetic jet actuator for aerodynamic stall control," *Computers & Fluids*, Vol. 35, No. 6, 2006, pp. 624–638. doi: 10.1016/j.compfluid.2005.01.005.

[6]Hassan, N., Kiedaisch, J., Greenblatt, D., Wygnanski, I., and Hassan, A., "Effective Flow Control for Rotorcraft Applications at Flight Mach Numbers," *AIAA paper 2001-2974*, 2001. doi: 10.2514/6.2001-2974.

[7]Gardner, A. D., Richter, K., Mai, H., and Neuhaus, D., "Experimental investigation of air jets for the control of compressible dynamic stall," *Journal of the American Helicopter Society*, Vol. 58, No. 4, 2013, pp. 1–14. doi: 10.4050/JAHS.58.042001.

[8]Seifert, A., David, S., Fono, I., Stalnov, O., Dayan, I., Bauminger, S., Guedj, R., Chester, S., and Abershitz, A., "Roll Control via Active Flow Control: From Concept Development to Flight," *49th Israeli Conference on Aerospace Engineering*, 2009.

[9]Seifert, A. and Pack, L. G., "Oscillatory Excitation of Unsteady Compressible Flows over Airfoils at Flight Reynolds Numbers," *AIAA Paper 99-0925*, 1999. doi: 10.2514/6.1999-925.

[10]Shmilovich, A. and Yadlin, Y., "Active Flow Control for Practical High-Lift Systems," *Journal of Aircraft*, Vol. 46, No. 4, 2009, pp. 1354–1364. doi: 10.2514/1.41236.

[11]Ciobaca, V., Dandois, J., and Bieler, H., "A CFD Benchmark for Flow Separation Control Application," *International Journal of Flow Control*, Vol. 6, No. 3, 2014, pp. 67–81. doi: ISSN 1756-8250.

[12]Ciobaca, V., Kühn, T., Rudnik, R., Bauer, M., and Gölling, B., "Active Flow-Separation Control on a High-Lift Wing-Body Configuration," *Journal of Aircraft*, Vol. 50, No. 1, 2013, pp. 56–72. doi: 10.2514/1.C031659.

[13]Schatz, M., Günther, B., and Thiele, F., "Computational Investigation of Separation Control for High-lift Airfoil Flows," *Active Flow Control. Notes on Numerical Fluid Mechanics and Multidisciplinary Design (NNFM)*, edited by R. King, Vol. 95, Springer Berlin Heidelberg, 2007, pp. 173–189.

[14]Höll, T., Kabat vel Job, A., Giacopinelli, P., and Thiele, F., "Numerical Study of Active Flow Control on a Hugh-Lift Configuration," *Journal of Aircraft*, Vol. 49, No. 5, 2012, pp. 1406–1422. doi: 10.2514/1.C031718.

[15]Nielsen, E. J. and Jones, W. T., "Integrated Design of an Active Control System Using a Time-Dependent Adjoint Method," *Math. Model. Nat. Phenom.*, Vol. 6, No. 3, 2011, pp. 141–165. doi: 10.1051/mmnp/20116306.

[16]Hall, K. C., Thomas, J. P., and Clark, W. S., "Computation of Unsteady Nonlinear Flows in Cascades Using a Harmonic Balance Technique," *AIAA Journal*, Vol. 40, No. 5, May 2002, pp. 879–886. doi: 10.2514/2.1754.

[17]Fleischer, D., Vidy, C., Iatrou, M., Breitsamter, C., and Weishäupl, C., "Linear Flutter Prediction for Low Aspect Ratio Wings Using a Small Disturbance Euler Method," *14th International Forum on Aeroelasiticity and Structural Dynamics*, IFASD Paper 2009-055, Seattle, WA, June 2009.

[18]Pechloff, A. and Laschka, B., "Small Disturbance Navier-Stokes Computations for Low-Aspect-Ratio Wing Pitching Oscillations," *Journal of Aircraft*, Vol. 47, No. 3, 2010, pp. 737–753. doi: 10.2514/1.45233.

[19]Widhalm, M., Dwight, R. P., Thormann, R., and Hübner, A. R., "Efficient Computation of Dynamic Stability Data with a Linearized Frequency Domain Solver," *5th European Conference on Computational Fluid Dynamics*, edited by J. C. F. Pereira and A. Sequeira, ECCOMAS CFD 2010, Lisbon, Portugal, June 2010.

[20]Ronch, A. D., Ghoreyshi, M., Badcock, K. J., Görtz, S., Widhalm, M., Dwight, R. P., and Campobasso, M. S., "Linear Frequency Domain and Harmonic Balance Predictions of Dynamic Derivatives," *28th AIAA Applied Aerodynamics Conference*, AIAA Paper 2010-4699, AIAA, Chicago, Illinois, 2010.

[21]Thormann, R. and Widhalm, M., "Linear Frequency Domain Predictions of Dynamic Response Data for Viscous Transonic Flows," *AIAA Journal*, Vol. 51, No. 11, Oct 2013, pp. 2540–2557. doi: 10.2514/1.J051896.

[22]Widhalm, M. and Thormann, R., "Efficient Evaluation of Dynamic Response Data with a Linearized Frequency Domain Solver at Transonic Separated Flow Conditions," *AIAA 2017-3905*, 2017, pp. 1–21. doi: 10.2514/6.2017-3905.

[23]Gerhold, T., Galle, M., Friedrich, O., and Evans, J., "Calculation of Complex Three-Dimensional Configurations Employing the DLR TAU-Code," *AIAA Paper 97-0167*, 1997. doi: 10.2514/6.1997-167.

[24]Schwamborn, D., Gerhold, T., and Heinrich, R., "The DLR TAU-Code: Recent Applications in Research and Industry," *Third European Conference on Computational Fluid Dynamics*, edited by P. Wesseling, E. Oñate, and J. Périaux, ECCOMAS CFD 2006, Egmond aan Zee, The Netherlands, Sept. 2006.

[25]Spalart, P. R. and Allmaras, S. R., "A One-Equation Turbulence Model for Aerodynamic Flows," AIAA Paper 92-0439, Jan. 1992.

[26]Allmaras, S. R., Johnson, F. T., and Spalart, P. R., "Modifications and Clarifications for the Implementation of the Spalart-Allmaras Turbulence Model," *Seventh International Conference on Computational Fluid Dynamics (ICCFD7)*, No. ICCFD7-1902, July 2012.

[27]Langer, S., Schwöppe, A., and Kroll, N., "The DLR Flow Solver TAU - Status and Recent Algorithmic Developments," *AIAA-Paper 2014-0080*, 2014. doi: 10.2514/6.2014-0080.

[28]Hirt, C. W., Amsden, A. A., and Cook, J. L., "An Arbitrary Lagrangian-Eulerian Computing Method for All Flow Speeds," *Journal of Computational Physics*, Vol. 14, No. 3, 1974, pp. 227–253. doi: 10.1016/0021-9991(74)90051-5.

[29]Jameson, A., "Time Dependent Calculations Using Multigrid with Applications to Unsteady Flows Past Airfoils and Wings," *AIAA 10th Computational Fluid Dynamics Conference*, AIAA Paper 91-1596, Honolulu, HI, June 1991.

[30]Mavriplis, D. J., "Multigrid Strategies for Viscous Flow Solvers on Anisotropic Unstructured Meshes," *Journal of Computational Physics*, Vol. 145, No. 1, Sept 1998, pp. 141–165. doi: 10.1006/jcph.1998.6036.

[31]Langer, S., Schwöppe, A., and Kroll, N., "Investigation and Comparison of Implicit Smoothers Applied in Agglomeration Multigrid," *AIAA Journal*, Vol. 53, No. 8, 2015, pp. 2080–2096. doi: 10.2514/1.J053367.

[32]Thomas, P. D. and Lombard, C. K., "Geometric Conservation Law and its Applications to Flow Computations on Moving Grids," *AIAA Journal*, Vol. 17, No. 10, 1979, pp. 1030–1037. doi: 10.2514/3.61273.

[33]Rumsey, C. L., Gatski, T. B., Sellers III, W. L., Vatsa, V. N., and Viken, S. A., "Summary of the 2004 CFD Validation Workshop on Synthetic Jets and Turbulent Separation Control," *AIAA Journal*, Vol. 44, No. 2, 2004, pp. 194–207. doi: 10.2514/1.12957.

[34]Knopp, T., "The actuation boundary condition for flow control in the DLR-TAU code," Tech. Rep. DLR-IB 224-2010 A 44, DLR-AS, 2010.

[35]Roe, P. L., "Approximate Riemann Solvers, Parameter Vectors, and Difference Schemes," *Journal of Computational Physics*, Vol. 43, 1981, pp. 357–372. doi: 10.1016/0021-9991(81)90128-5.

[36]Turkel, E., "Improving the Accuracy of Central Difference Schemes," Tech. Rep. 88-53, ICASE, 1988.

[37]Langer, S., "Investigation and application of point implicit Runge-Kutta methods to inviscid flow problemspplication of Point Implicit Runge-Kutta Methods to Inviscid Flow Problems," *International Journal for Numerical Methods in Fluids*, Vol. 69, No. 2, 2011, pp. 332–352. doi: 10.1002/fld.2561.

[38]Hussein, H. J., Capp, S. P., and George, W. K., "Velocity measurements in a high-Reynolds-number, momentum-conserving, axisymmetric, turbulent jet," *J. Fluid Mech.*, Vol. 258, 1994, pp. 31 – 75. doi: 10.1017/S002211209400323X.

[39]Dwight, R. and Brezillon, J., "Effect of Approximations of the Discrete Adjoint on Gradient-Based Optimization." *AIAA Journal*, Vol. 44, No. 12, Dec 2006, pp. 3022–3031. doi: 10.2514/1.21744.

[40]Cooley, J. W. and Tukey, J. W., "An Algorithm for the Machine Calculation of Complex Fourier Series," *Mathematics of Computation*, Vol. 19, No. 90, 1965, pp. 297–301. doi: 10.2307/2003354.

[41]Saad, Y. and Schultz, M. H., "GMRES: A Generalized Minimum Residual Algorithm for Solving Nonsymmetric Linear Systems," *SIAM Journal of Scientific and Statistical Computing*, Vol. 7, No. 3, 1986, pp. 856–859. doi: 10.1137/0907058.

[42]Saad, Y., *Iterative Methods for Sparse Linear Systems*, Society for Industrial and Applied Mathematics, 2nd ed., 2003.

[43]McCracken, A. J., Ronch, A. D., Timme, S., and Badcock, K. J., "Solution of linear systems in Fourier-based methods for aircraft applications," *International Journal of Computational Fluid Dynamics*, Vol. 27, No. 2, Jan. 2013, pp. 79–87. doi: 10.1080/10618562.2012.750719.

[44]Thormann, R. and Widhalm, M., "Forced Motion Simulations using a Linear Frequency Domain Solver for a Generic Transport Aircraft," *16th International Forum of Aeroelasticity and Structural Dynamics*, IFASD 2013-017A, Bristol, UK, 2013.

[45]Xu, S., Timme, S., and Badcock, K. J., "Enabling off-design linearised aerodynamics analysis using Krylov subspace recycling technique," *Computers & Fluids*, Vol. 140, 2016, pp. 385–396. doi: 10.1016/j.compfluid.2016.10.018.

[46]Poisson-Quinton, P., "Recherches théoriques et expérimentales sur le contrôle de couche limite," *7th Congress of Applied Mechanics*, London, September 1948.

[47]Pinkerton, R. M., "Calculated and Measured Pressure Distributions over the Midspan Section of the NACA 4412 Airfoil," Tech. Rep. NACA-TR-563, NASA Langley Research Center, 1936.

[48]Camocardi, M. E., Marañon Di Leo, J., Delnero, J. S., and Colman Lerner, J. L., "Experimental Study of a NACA 4412 Airfoil with Movable Gurney Flap," *AIAA Paper 2011-1309*, 2011. doi: 10.2514/6.2011-1309.

[49]Wild, J., "Experimental investigations of Mach- and Reynolds-number dependencies of the stall behavior of 2-element and 3-element high-lift wing sections," *AIAA Paper 2012-108*, 2012. doi: 10.2514/6.2012-108.

American Institute of Aeronautics and Astronautics